HENRIQUE SÉRGIO GUTIERREZ DA COSTA

BIOMETRIC IDENTIFICATION WITH 3D FINGERPRINTS ACQUIRED THROUGH OPTICAL COHERENCE TOMOGRAPHY

Thesis presented to Programa de Pós-Graduação em Informática at Universidade Federal do Paraná

Supervisor: Prof.Luciano Silva to obtain the doctoral degree

Co-Supervisor: Prof. Olga Regina Pereira Bellon

Curitiba, Pr

2016

MINISTÉRIO DA EDUCAÇÃO
UNIVERSIDADE FEDERAL DO PARANÁ
PRÓ-REITORIA DE PESQUISA E PÓS-GRADUAÇÃO
Setor CIÊNCIAS EXATAS
Programa de Pós Graduação em INFORMÁTICA
Código CAPES: 40001016034P5

TERMO DE APROVAÇÃO

Os membros da Banca Examinadora designada pelo Colegiado do Programa de Pós-Graduação em INFORMÁTICA da Universidade Federal do Paraná foram convocados para realizar a arguição da Tese de Doutorado de **HENRIQUE SERGIO GUTIERREZ DA COSTA**, intitulada: "**BIOMETRIC IDENTIFICATION WITH 3D FINGERPRINTS ACQUIRED THROUGH OPTICAL COHERENCE TOMOGRAPHY**", após terem inquirido o aluno e realizado a avaliação do trabalho, são de parecer pela sua APROVAÇÃO.

Curitiba, 28 de Junho de 2016.

Prof LUCIANO SILVA
Presidente da Banca Examinadora (UFPR)

Prof ANDRÉ LUIZ PIRES GUEDES
Avaliador Interno (UFPR)

Prof EDUARDO PARENTE RIBEIRO
Avaliador Externo (UFPR)

Prof LUIZ ANTÔNIO PEREIRA NEVES
Avaliador Externo (UFPR)

Olga Regina Pereira Bellon
Prof OLGA REGINA PEREIRA BELLON
Coorientador - Avaliador Interno (UFPR)

Audrey Bowden
Prof AUDREY K BOWDEN
Avaliador Externo (SFU)

CONTENTS

Index of Figures

Index of Tables

Table of Acronyms

ERR	Equal Error Rate
CCD	Charge Coupled Device
CMC	Cumulative Matching Characteristic
CL	Cylindrical Lens
COMPDC	Compatibility Database
CORR2D	2D Normalized Cross-Correlation
EURODAC	European Asylum Seeker register
DLP	Digital Light Processing
FAR	False Acceptance Rate
FD-OCT	Fourier-domain Optical Coherence Tomography
FF-OCT	Full-field Optical Coherence Tomography
FRR	False Rejection Rate
LED	Light Emitting Diode
LGP	Local Gradient Patterns
NIST	National Institute of Standards and Technology
OCT	Optical Coherence Tomography
OCTDB	Optical Coherence Tomography 3D Fingerprint Database
OFDI	Optical frequency Domain Interferometry
POLYUDB	The Hong Kong Polytechnic University 3D Fingerprint Images Database
PPI	Pixels Per Inch
RMS	Root Mean Square
ROC	Receiver Operating Characteristic
ROI	Region of Interest
SD-OCT	Spectral Domain Optical Coherence Tomography
SLD	Superluminescent Diode
SNR	Signal-to-noise Ratio
SS-OCT	Swept-source Optical Coherence Tomography
TD-OCT	Time-domain Optical Coherence Tomography

RESUMO

Um método para se obter impressões digitais 3D da derme e da epiderme a partir de imagens em alta resolução adquiridas utilizando Tomografia de Coerência Ótica (OCT) é proposto neste trabalho. Este método, resolve limitações das técnicas de reconstrução 3D de impressões digitais que empregam múltiplas câmeras/triangulação ou iluminação estruturada, tais como variações de resolução do centro para as bordas das impressões digitais 3D causadas por erros de reconstrução, sensibilidade a baixa iluminação e contraste insuficiente.

Uma técnica de busca e identificação baseados em padrões inovativos, os “mapas KH ” (usados para a segmentação de regiões de superfície em imagens de intensidade e de profundidade), extraídos computando as curvaturas Gaussiana (K) e média (H) de uma região de interesse na vizinhança das minúcias (denominada nuvem de minúcia), é apresentada. Grandes bases de mapas KH, uma para cada nuvem de minúcia identificada, podem ser construídos com essa técnica. A estratégia de busca e identificação, em duas etapas, baseia-se primeiro em padrões locais de gradientes (LGP) dos mapas KH, para reduzir o espaço de busca dentro da base, seguidos de uma comparação que utiliza uma medida de similaridade, a correlação cruzada normalizada dos padrões pré-selecionados com o LGP com os que se quer identificar. A acuracidade do método e sua compatibilidade com os métodos correntes, comparável ou superior à dos métodos 2D, é verificada através da identificação biométrica de impressões digitais 3D utilizando duas bases de imagens, uma adquirida através da tecnologia OCT e a outra gentilmente cedida pela Universidade Politécnica de Hong Kong.

A base de imagens OCT, a primeira adquirida com essa tecnologia, é composta de imagens coletadas de onze voluntários em duas sessões de escaneamento e contém imagens de dedos de pessoas com diferentes idades, gênero e etnias e contém casos de cicatrizes, calos e alterações, tais como abrasão e arranhões. Uma base de impressões digitais 2D, obtida dos mesmos voluntários através de um leitor regular de impressões digitais, foi adquirida para permitir uma comparação da técnica proposta com os métodos de identificação tradicionais.

A aplicabilidade do método proposto à identificação de impressões digitais alteradas, deterioradas acidentalmente ou intencionalmente, é investigada. Nesses casos, a impressão digital 3D extraída da derme e compatível com a da epiderme é empregada. A identificação destas impressões 3D alteradas é testada utilizando a base de imagens adquiridas com OCT. A acuracidade da técnica é comparada com a obtida utilizando os métodos tradicionais 2D usando os gráficos de taxas de Falsa Aceitação e Falsa Rejeição (FAXxFRR) e de Características Cumulativas de Identificação (CMC). Impressões digitais 2D, extraídas a partir das impressões digitais 3D simulando o rolamento do dedo durante a aquisição (rolamento virtual), foram geradas e sua compatibilidade com as bases de imagens 2D foi testada.

Um conjunto de medidas de avaliação de qualidade foram aplicados às bases de imagens de impressões digitais 3D e sua correspondência aos escores de identificação foi analisada para determinar aqueles que podem contribuir para melhorar a acuracidade da identificação.

Palavras-chave: Impressões digitais 3D. Identificação Biométrica. Tomografia de Coerência Ótica.

ABSTRACT

A method to obtain epidermal and dermal 3D fingerprints from high-resolution images acquired using Optical Coherence Tomography (OCT) is proposed. This method addresses limitations of current 3D reconstruction techniques that employ multiple cameras/triangulation or structured illumination such as depth and resolution variations from the center to the borders of the fingerprint caused by reconstruction errors, sensitivity to low illumination and poor contrast. The availability of these 3D fingerprints allowed the creation of new matching methods that benefit from the rich information available in 3D.

A 3D fingerprint matching technique based on novel patterns, the KH maps (used to surface region segmentation in range and intensity images), extracted by computing the Gaussian and mean curvatures (SILVA; BELLON; GOTARDO, 2001) from a region of interest around the minutiae, named *minutiae clouds* is presented. Large databases of KH maps, one for each identified minutiae cloud can be built. The matching strategy, a two-step approach, relies on local gradient patterns (LGP) of the KH maps to narrow the search space, followed by a similarity matching, the normalized cross correlation of patterns being matched. The accuracy and matching compatibility, comparable or improved in relation to the 2D matching methods, is verified through matching 3D fingerprints from two databases one acquired using OCT and a public database gently made available by the Hong Kong Polytechnic University.

The OCT database, the first 3D database acquired using Optical Coherence Tomography, to our knowledge, is made of images collected from eleven volunteers in two scanning sessions and contains images of people of different ages, genders and ethnicities and also cases of scars, calluses and alterations as abrasion and scratches. A 2D fingerprint database, scanned from the same volunteers using a regular fingerprint reader was also obtained for comparison with traditional matching methods.

We investigate the applicability of our method to the identification of altered fingerprints, damaged unintentionally or accidentally. In these cases, the 3D dermal fingerprint, compatible with the epidermis fingerprint, is employed. Matching with 3D dermal and epidermal fingerprints is tested in the OCT database. Matching accuracy is compared with the obtained using traditional matching 2D methods by using False Acceptance and False rejection rate (FARxFRR) and Cumulative Matching Characteristics (CMC) graphs. Unwrapped fingerprints, 2D fingerprints extracted from 3D fingerprints by virtual unrolling were generated and tested for compatibility with 2D databases.

A set of quality evaluation measures were employed to the 3D fingerprint databases and their correspondence to the matching scores was analyzed to identify those that can contribute to improve the matching accuracy.

Key-words: 3D Fingerprints. Biometric identification. Optical Coherence Tomography.

1 - INTRODUCTION

The identification of human beings has been used for many years in commercial, governmental and legal applications such as checking if the identity claimed by the individual is true by comparing its features to previously stored ones or identifying if these features could be found within a database. Many personal attributes such as fingerprints, iris, signature, retina, ear shape, hand veins, gait, palm print and people odor have been used individually or combined (multibiometrics). Fingerprint based biometric systems rely on image features present in the finger skin, such as the ridges and valleys patterns, minutiae, texture and sweat pores.

A particular use of these technologies, that is gaining importance due to the increasing number of identification deception attempts (FENG; JAIN; ROSS, 2010; YOON; FENG; JAIN, 2012), is border control and access to security facilities, which are in crescent demand for governmental and civilian applications. 2D fingerprint technologies have been successfully used for years but despite the continuous improvement, such as the adoption of more discriminant information of sweat pores and ridge textures, some opportunities for improvement remain. It has been estimated that 4% of the population (JAIN; ROSS; PRABHAKAR, 2004) may have poor skin ridge quality making it difficult to scan these fingerprints. One of the current issues is vulnerability to skin alterations, which can negatively affect the identification systems performance. Alterations can be unintentional, as in the cases of abrasion and cutting, or deliberate, as the cases of acid burns and plastic surgery with the purpose of evading the identification by a biometric system , as described by Yoon and Jain (YOON; FENG; JAIN, 2012). Another case of relevance is the identification of corpses, whose skin alteration is caused by the putrefaction or damage to the skin by accidents or catastrophes. In this case, the dermal fingerprint is usually employed, after exposed through a chemical process (MIZOKAMI; SILVA; KÜCKELHAUS, 2015).

The identification of newborn babies is considered a challenging problem due to its high deformability, the small dimensions of their dermatoglyphics. The use of current contact-based fingerprint scanners, whose resolution is typically 500 dpi, is not suited to these individuals for the mentioned reasons. Resolution greater than 1,500 dpi to imaging newborn babies fingerprints is recommended (WEINGAERTNER, 2007), since papillary ridges width is approximately 0.10 mm (CUMMINS; MIDLO, 1976) and 2,250 dpi to premature babies is suggested as their ridge with is even smaller. Skin deformability was attributed to the small thickness of the epidermis, in contrast with the dermis, more dense and less deformable, as tested in (GUTIERREZ DA COSTA; MAXEY; SILVA; ELLERBEE, 2014) and can be prevented by scanning without the need to have the contact of finger skin with the scanner.

The use of 3D fingerprint geometry has been studied as a promising alternative to 2D identification technologies as it provides richer discriminatory information obtained through contactless imaging and 3D reconstruction. However, despite their inherent advantages as the immunity to skin deformation, it has been limited to superficial images of the skin, i.e. the *stratum corneum*, which can be impacted by illumination, brightness, contrast, and errors inherent to triangulation (in multiple camera implementation) or phase-calculation (in structured light illumination techniques) such as ridge/valley depth variations and resolution variation from the center to the borders of the 3D images (PARZIALE, 2008). The use of 3D scanners that provide the spatial information directly, with no need of reconstruction from 2D images, can potentially minimize the errors inherent to these techniques. By working with the 3D information, one can use it to matching directly or extract some discriminant characteristic such as curvatures.

A new method to obtain 3D fingerprints from images of the dermis and epidermis, acquired through Optical Coherence Tomography, by detecting the signal intensity changes caused by variations in the refractive index of the skin layers is proposed. Optical Coherence Tomography, a contactless high-resolution scanning technology that acquires in-depth 3D images of the skin layers allows obtaining images of the internal structures of the skin, exposing information that can be potentially be used to improve identification or verification if compared to traditional 2D fingerprint identification methods and help identifying fake fingerprints. The resolutions obtained (of less than 1μm in some configurations) are sufficient to scan newborn babies' fingerprints and the use of the information available in the dermis-epidermis interface can be make possible biometric identifications when the epidermis has been altered. In addition , the skin intensity profile (signal intensity with depth) and the internal structures of the skin can be used to detect fake fingerprints or evidence of fingerprint alteration (CHENG; LARIN, 2006), (MEISSNER; BREITHAUPT; KOCH, 2013a).

In our method, 3D point clouds (3D fingerprints) are extracted from the epidermis and dermis-epidermis of OCT images and a region of interest (ROI), a small point cloud around fingerprint minutiae, named *minutiae cloud* is cut. From the points of this ROI, the distinctive information that will be used for biometric identification is calculated by using the gradients of each point and its neighbors. The use of multiple minutiae clouds can improve the accuracy of the biometric identification if compared to the traditional 2D methods. A database of epidermal and dermal OCT 3D fingerprints, the first to our knowledge, was built by scanning images of eleven volunteers in two sessions held in different days, following a protocol approved by Stanford University, where the images were collected. The volunteers, of various ethnicities and ages had their ten fingers scanned.

A method for fingerprint matching based on the mentioned novel patterns is also presented. The patterns used for matching, KH maps, are shown in Fig.1, being computed from minutiae clouds based on signs of the Gaussian and mean curvatures as proposed by (BESL; JAIN, 1986). Large databases of KH maps, one for each identified minutiae cloud, can be built, what can impact the matching response time. The matching strategy, a two-step approach relies on local gradient patterns (LGP) of the KH maps to mitigate this problem by narrowing the search space, followed by a similarity matching of the nearest neighbors of the pattern being searched. Our proposed method addresses the problem of extracting 3D features and exploiting them for improved matching in large databases. The accuracy and matching compatibility, comparable or improved in relation to the 2D matching methods is verified through matching using epidermis-epidermis and dermis-epidermis minutiae clouds and comparing the results (FARxFRR, ROC and CMC curves) with those obtained for traditional 2D fingerprint matching collected from the same volunteers.

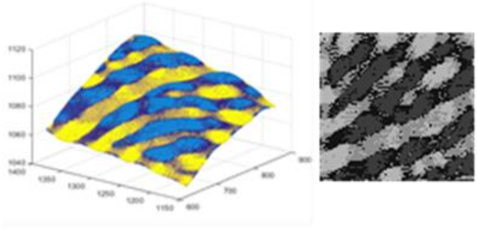

(a) (b)

Fig. 1- KH map:(a) 3D plotting, colors correspond to curvature types (light blue-peak, dark blue-saddle ridge, yellow-pit and orange-saddle valley) and (b) 2D representation

We also investigate the applicability of our method to the identification of altered fingerprints, damaged unintentionally or accidentally. In these cases, the 3D dermal fingerprint, compatible with the epidermis fingerprint, is employed and the KH maps extracted from them.

Finally, a test of the applicability of the proposed matching technique to 3D fingerprints acquired through other acquisition methods has been conducted and the results presented.

2 - PERSON IDENTIFICATION USING FINGERPRINTS

Personal identification based on physical or behavioral attributes of the individual is largely used for commercial, governmental and legal applications. The most frequent situations are: *verification, i.e.* checking if the identity claimed by the individual is true by comparing its features against previously stored ones (a 1:1 comparison with features of the same individual) or identification, matching the features to the ones stored in a database (a 1:N comparison). In both fingerprint-based identification and verification, the dermatoglyphics, finger skin patterns present in the skin, are used.

Dermatoglyphics and Ridge Formation

Fingerprints are formed by the detection (by an image sensor or ink and paper printing) of the finger dermatoglyphics, present in the outer layer of the epidermis of the hands, palmprints and soles. The epidermis is divided in several layers, being the *stratum corneum*, the outermost. This layer is made of dead, hardened cells., constantly removed by the use of hands. It is originated by the migration of cells from the deepest part of the epidermis, where the living cells are constantly multiplying to replace the lost cells of the *stratum corneum*. During this migration, the epidermal cells get hardened (CUMMINS; MIDLO, 1976) .

The epidermal- dermal interface is not smooth, having irregularities that, in the dermis are named *dermal papillae*, made of connective tissue. The occurrence of the epidermal ridges is determined during the fetus formation, caused by the proliferation of the cells into the epidermis , which is invaded and molded by the *dermal papillae* (CUMMINS; MIDLO, 1976). The process is also influenced by the flow of the amniotic fluids around the fetus and its position within the uterus, making it virtually impossible for two individuals to have the same configuration, although genetic influence could be observed between identical twins (D.MALTONI, A.JAIN, D.MAIO, 2003), case where a strong similarity occurs.

Alterations

Finger skin alteration can occur for several reasons, one example is related to the constant use of the hands in labor activities that change the structure of the skin ridges (JAIN; ROSS; PRABHAKAR, 2004), (FENG; JAIN; ROSS, 2010) another is the intentional alteration of the skin to try to mask a person identity through burns, cuts, abrasion and even plastic surgery. These changes can alter the shape of the fingerprints scanned by traditional, contact-based or even contactless scanners and deceive the automatic identification systems, problem known as biometric *obfuscation* (YOON; FENG; JAIN, 2012). Since the quality of the resulting altered fingerprints is not always lowered, the use of quality measures of the fingerprints is, in many cases, ineffective to detect alteration.

Alterations can generally be classified in three types, Obliteration, Distortion and Imitation (SELVARANI; JEBAPRIYA; MARY, 2014). *Obliteration*, is caused by abrading, burning, cutting or applying chemicals in an attempt to wipe out or make the fingerprint indistinguishable. *Distortion* is the change of ridge patterns into unnatural ones, by cutting or replacing finger pads of one finger by skin removed from other finger or from other parts of the body as the palms and soles. *Imitation* is an alteration that does not change the ridge patterns. It is made by removing a part of the skin and stitching the remaining part together or by swapping finger tips of two different fingers.

3 - BIOMETRIC IDENTIFICATION / VERIFICATION SYSTEMS

The automated identification of a person is usually made through biometrical systems. These are described by (JAIN; ROSS; PRABHAKAR, 2004) as pattern recognition systems that acquires biometric data from a person, extracts a particular feature set from the data, compares it against the ones stored in a database and executes some action, depending on the comparison result.

These systems must satisfy the following conceptual requirements (Table I) (JAIN; ROSS; PRABHAKAR, 2004), (LI; JAIN, 2009): *universality* (every individual has the biometrical characteristic used by the system), *distinctiveness* (the characteristic is different if two individuals are compared), *permanence* (the characteristic should not change with the time), *collectability* (the characteristic can be measured). In addition, other practical requirements are relevant, as the *performance* (speed and accuracy), *acceptability* (people willingness to accept the use of such biometric identification/verification in their lives) and *circumvention* (immunity to fraud).

Table I – Comparison of biometrics technologies based on the perceptions of three experts. H means high, M means Medium and L means Low (JAIN; ROSS; PRABHAKAR, 2004).

Biometric Trait	Universality	Distinctiveness	Permanence	Collectability	Performance	Acceptability	Circumvention
DNA	H	H	H	L	H	L	L
Ear shape	M	M	H	M	M	H	M
Face	H	L	M	H	L	H	H
Facial Thermogram.	H	H	L	H	M	H	L
Fingerprint	M	H	H	M	H	M	M
Gait	M	L	L	H	L	H	M
Hand Geometry	M	M	M	H	M	M	M
Hand veins	M	M	M	M	M	M	L
Iris	H	H	H	M	H	L	L
Keystrokes	L	L	L	M	L	M	M
Odor	H	H	H	L	L	M	L
Palm print	M	H	H	M	H	M	M
Retina	H	H	M	L	H	L	L
Signature	L	L	L	H	L	H	H
Voice	M	L	L	M	L	H	H

By observing Table, I, it is possible to conclude that no biometric system fully satisfies all the requirements. To improve the performance of such systems, approaches using multi-biometric identification by fusing information from multiple biometric sources (CHANG; XIAOQING, 2006; POH; ROSS; LEE; KITTLER, 2013) are employed. An alternative is to improve the matching accuracy by the use of new biometric information as 3D fingerprints since they are universal and permanent and the availability of 3D much richer information (if compared with 2D) can increase the distinctiveness. If added the capture of inner skin layer structures, improvement in the circumvention characteristics can also be obtained.

In general, biometrical systems can be viewed as a combination of modules: an image acquisition device (where the images are collected), a processing and feature extraction stage (where tasks as de-noising, image registration, quality evaluation, feature extraction and database construction occur) and an identification/verification stage, where matching by comparing the image from user to the ones stored in a database is executed (JAIN; ROSS; PRABHAKAR, 2004), as in Fig. 2.

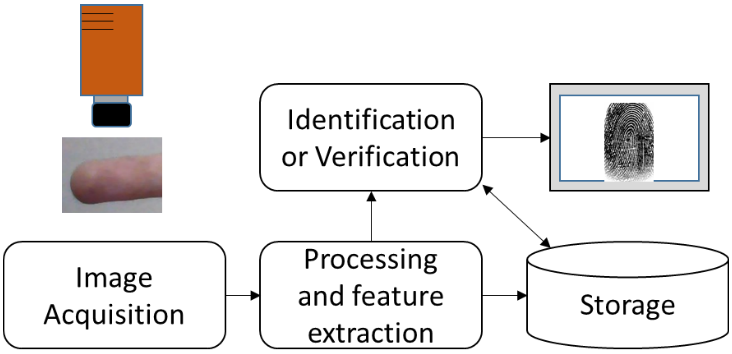

Fig. 2 – Biometric System Modules

In the next session, 3D Image Acquisition literature is reviewed and a detailed description of Optical Coherence Tomography (OCT) technology is presented.

4 - ACQUISITION OF 3D FINGERPRINTS

3D acquisition systems have been proposed in the literature: in (PARZIALE; DIAZ-SANTANA; HAUKE, 2005) a touchless scanner with 5 cameras and an array of 16 LEDs (light emitting diodes) obtains 3D reconstructed images using stereovision and photogrammetry-based algorithms from 2D images. Minutiae coordinates (x, y, z) and their azimuthal and zenithal angles are employed to find the correspondent points between pairs of 2D images scanned. This information and the 3D shape estimation (using “shape from silhouette” technique), are needed for 3D reconstruction. The matching process employs 2D and 3D features: 2D matching is computed using unwrapped images (from the 3D reconstructed fingerprints) and 3D matching uses correspondent spatial minutiae triangles.

In (HUANG; ZHANG; ZHAO; DAI; … XIE, 2014), a sinusoidal pattern is projected by a digital light processing (DLP) device on the finger. Images of the projection of these patterns are captured by a CCD and the phase change in relation to the projected pattern is recovered by a four-step algorithm and a technique named “optimum three fringe number selection”. A calibration method recovers the depth (z) and x-y positions to the 3D reconstruction of the fingerprint. Additional processing as calibration (to compensate for optical system and projector errors), phase calculation, phase unwrapping, optimum three fringe number selection and reconstruction are needed. Errors of 0.0301 mm in depth and 0.0006 mm in *x* and 0.014mm in *y* were found, in relation to the golden standard adopted. Matching results were not presented in this work.

(WANG; HASSEBROOK; LAU, 2010) used structured light illumination (SLI) and phase measuring profilometry to obtain a 3D model of the finger. An unwrapped 2D fingerprint is built through a deformable tube parametric technique (where each transversal section of the 3D fingerprint at a given height is unwrapped on a cylindrical surface). The final 2D fingerprint can use ridge depth, albedo or a combination of both. Quality evaluation and matching has shown that the best quality 2D fingerprints were obtained when the combined strategy (ridge depth and albedo) is adopted.

In (LABATI; GENOVESE; PIURI; SCOTTI, 2016), whose focus was in the acquisition with moving fingers, two images are collected and enhanced to increase fringe contrast, they are rotated to align to the Y Cartesian axis and correspondent points of the two images (obtained by two cameras) are found using block matching and normalized cross-correlation. A 3D shape is computed by triangulation using the coordinates of the corresponding points; an image of the ridge pattern texture is superimposed to the 3D model. Unwrapped images are obtained by rotating the model at a constant regular angle pitch and resampling the texture image at a constant step. These images are used for matching, having obtained an EER of 0.09% and FMR of 0.12%. However, those rates worsened with intentional misplacements and rotations of the finger to respectively 2.40% and 1.2%. When the compatibility with flat 2D fingerprints was tested, the EER was 1.48% in one of the tested datasets in the worst case. The 3D reconstructed model does not have the ridges and valleys depth information, only the finger shape superposed by the ridge/valley texture.

A different approach, using a single camera and seven LEDs was described in (KUMAR; KWONG, 2013) and (KUMAR; KWONG, 2015). Seven 2D images obtained by synchronized flashing of the LEDs at different angles in relation to the finger are used to build a 3D fingerprint (approximated to a Lambertian surface) using the shape from shading technique, least squares technique and a Poisson solver. For matching, the surface curvatures maximum and minimum are calculated and used to compute a shape index (SI). Depending on the value of SI, the surface is segmented in five types (cup, rut, saddle, ridge, cap). This index is combined with the direction of the dominant principle curvature (out of six possible directions) to form a representative vector of the surface, named Finger Code. Normalized Hamming distance between the surface codes of two different 3D fingerprints is used for 3D matching. The 3D coordinates, including the height (in spherical coordinates) and the angles in relation to a central minutia, adopted as a reference are also employed for matching through the calculation of a score based on the amount of matched minutiae. 2D camera images were used to construct the 3D fingerprint are also to 2D matching. Attempts to unwrap the 3D image to generate a compatible 2D fingerprint resulted in excessive distortions, if compared to 2D fingerprints obtained from 3D models using structured light (adopted as the golden standard) what prevented its use for matching. A database of 3D fingerprints from 240 users was built. 3D fingerprint matching using the curvatures obtained an EER of 15.56%.The best matching results were obtained when 3D minutiae was fused with 2D minutiae-based scores (adaptive fusion), achieving an EER 1.02% (KUMAR; KWONG, 2015). Reconstruction errors and differences of height between the center and the edges of the fingerprint were reported as detrimental to matching performance.

In (LIU; ZHANG, 2014), the images are obtained through three cameras and three LEDs. The 3D image reconstruction is done first by finding SIFT features and minutiae correspondence between the collected 2D images, then fitting the points to a shape model (quadratic model in the transversal direction and logarithmic in the longitudinal direction). Reconstruction errors between the obtained 3D fingerprints and the ground truth (images obtained by structured light illumination) of up to 0.35 mm were found. Curve skeletons extracted from these 3D images (LIU; ZHANG; SHEN, 2015) are used for matching along with curvature maximum and minimum measures. The curvature shape matching (mean distance between sets and matched points, obtained through Iterative Closest Points) alone resulted in EER of 15%, improved to 3.4% when the curvature measures were included. The maximum curvature was also used to gender classification.

The mentioned acquisition/3D reconstruction techniques can be classified in two categories: *structured light illumination followed by phase detection* and *depth calculation or triangulation-based* to find the corresponding points of multiple images and shape estimation.

The matching methods can be classified as: 1) 2D-based using unwrapped images obtained from the 3D fingerprint models or from the original 2D images themselves; 2) Purely 3D, by using the 3D minutia linear and angular positioning; curvature-based features or a combination of them with 2D matching (usually minutiae) features. A set of common problems to the listed 3D reconstruction methods was reported: depth errors due to the reconstruction method used; depth difference from the center to the image borders; ridge width variation from the center to the border of image; correspondence error between 2D fingerprints due to small overlapping, poor illumination/low-contrast and different resolutions from the center to the image borders.

In the following session, Optical Coherence Tomography (OCT), the technology selected to acquire the 3D Fingerprints used in this research is detailed and its robustness to the mentioned problems explained due through its different acquisition principle that relies on light interference to obtain directly acquired images and does not require 3D reconstruction. In addition, OCT allows high resolution touchless acquisition of the internal layers of the skin which can contribute to the solve the problem of biometric identification in the presence of alterations listed in the Introduction.

5 - OPTICAL COHERENCE TOMOGRAPHY

Optical Coherence Tomography can generate 2D cross-sectional images or 3D images of the skin and has been used in the biomedical area to image structures a few millimeters deep with submicron resolution (BOUMA, B.E.TEARNEY, 2002) as shown in Fig.3. Low time-coherent light in the near infrared wavelength range (700 to 1,300 nm) (WOJTKOWSKI; SRINIVASAN; KO; FUJIMOTO; KOWALCZYK; DUKER, 2004) and low optical power are used (FERCHER, 2010). This technology, suited to skin imaging, has been applied to the dermatology field in monitoring of wound healing, inflammatory skin diseases and tumor diagnosis. The use of OCT to image the skin have been published in several works (ZAKHAROV; TALARY; KOLM; CADUFF, 2009), (HOJJATOLESLAMI; AVANAKI, 2012), (YANG; CHEN, 2010) . In the biometric identification area, research regarding the detection fake fingerprints using this technology has been published (GALBALLY; CAPPELLI; LUMINI; GONZALEZ-DE-RIVERA; MALTONI; FIERREZ; ORTEGA-GARCIA; MAIO, 2010; MEISSNER; BREITHAUPT; KOCH, 2013b), (CHENG; LARIN, 2006),(NASIRI-AVANAKI, 2011), (DARLOW; CONNAN, 2015),(BREITHAUPT; SOUSEDIK; MEISSNER, 2015).

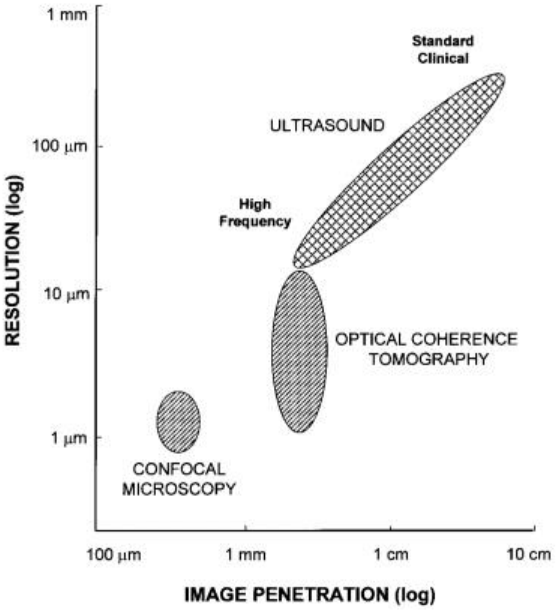

Fig. 3 – OCT and other medical imaging modalities

OCT is based on the low coherence interferometry, i.e. the interference of two light beams with low time coherence. Low time coherence light sources are the ones whose phase of the light wave can be reasonably predicted (HECHT, 2002) within a short period of time.

Such time is related to the bandwidth of the light source Δυ. If the source is perfectly monochromatic Δυ=0, the coherence time is infinite, in practice partial coherence (quasi-monochromatic light sources whose bandwidth is limited) or no coherence if found (which is the case of natural light in general). The short time coherence is used to acquire images to select the scanning depth in traditional time domain OCT.

OCT implementations are usually based on an interferometer. In Fig. 4 the basic configuration of a Michelson interferometer (used in OCT), is shown. Low-coherence light beam (from the light source) is divided (by a beam splitter) in two beams (reference beam and sample beam), one directed to a mirror (reference mirror) and other to the sample. After reflecting in the reference mirror and in the sample, the beams are recombined in the beam splitter and interfere in a light detector or a camera, where the depth information can be obtained. The depth signal (interference signal) is proportional to the intensity reflected from the internal layers of the sample at a certain depth and amplitude is obtained after processing in a computer. The coherence depth can be changed by moving the reference mirror in the traditional OCT (in time-domain configuration) or using through the reflected light bandwidth, scanned by a spectrometer (in Fourier-domain configuration).

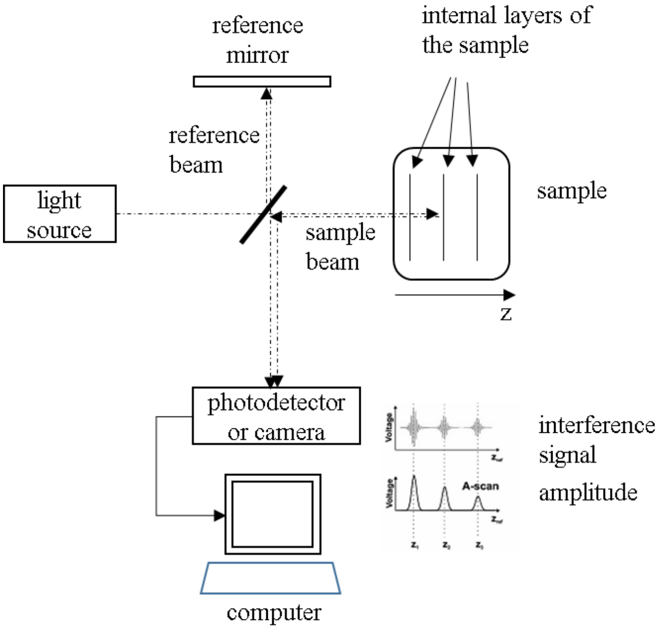

Fig. 4 – Basic OCT implementation using a Michelson interferometer

The signal amplitude graph in the figure refers to the scanning of a single line of the sample in depth of (from depths 0 to z_{max}). This scanned signal is known as A-scan (axial scan). A transversal cross-section of the image can be obtained by scanning several A-scans in a row, representation known as a B-scan as in Fig 5.a. B-scans can be stacked to build a 3D volume, as shown in Fig.5.b.

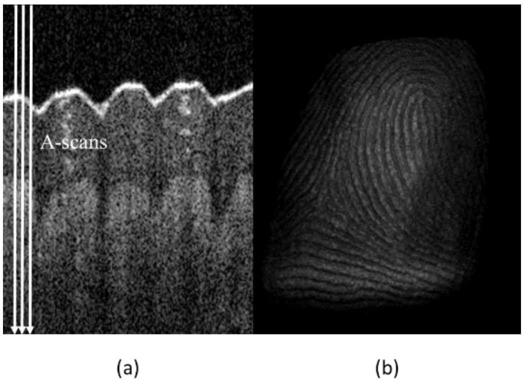

Fig. 5 – Skin images acquired by OCT: (a) B-scan of the skin(a), the white arrows in white detail of some A-scans;(b) a 3D image (volume)

OCT Implementation Schemes

OCT implementation schemes can be classified in two domains: *Time-Domain* (TD-OCT) and *Fourier Domain* (FD-OCT). These differ in way that the depth information is recovered and, as a consequence, in some of their system components (as spectrometers, tunable lasers and translation stages), and in performance parameters as sensitivity and acquisition speeds (LEITGEB; HITZENBERGER; FERCHER, 2003). In general FD-OCT has less moving parts to scanning in depth.

Time Domain is the traditional OCT technology and relies on low coherence interferometry (LCI). The depth scan is obtained by the translation of a mirror (as shown in Fig. 4) and, if a point-scan is used (scanning point by point), the lateral scan is usually done using a X-Y translator to move the scanning probe or the sample (in this case keeping the probe in a fixed position) i.e. scanning a point at a time is adopted. If an area scanning is adopted, an implementations known as Full-Field OCT (FERCHER; DREXLER; HITZENBERGER; LASSER, 2003), studied in this research work, can be adopted (Fig.6).

Full-field OCT (FF-OCT) is capable of scanning large areas (of a few tens of millimeters) requiring only the translation of the reference mirror to obtain the depth scan. In this case, the collected images are acquired in planes parallel to the objective lens, called en-Face images (as shown in Fig.7). To obtain a large field of view (in a configuration known as Wide-field) , low numerical aperture objective lens is usually adopted as in (FEDERICI, A., COSTA, H.S.G, DUBOIS, OGIEN, J., ELLERBEE,A.K., DUBOIS,A., 2015).

Two factors limit the use of FF-OCT, slow acquisition speeds resulting from the need to execute a mechanical translation of the reference mirror to depth scanning and the need to accumulate (add) images to improve the sensitivity (DUBOIS, ARNAUD;BOCCARA, 2008).

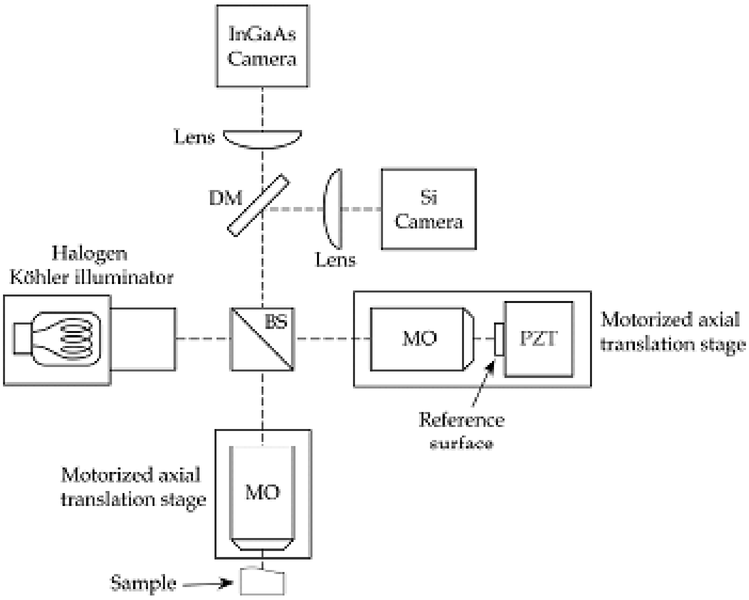

Fig. 6 – Full-Field (TD) typical configuration. From: (DUBOIS, 2001)

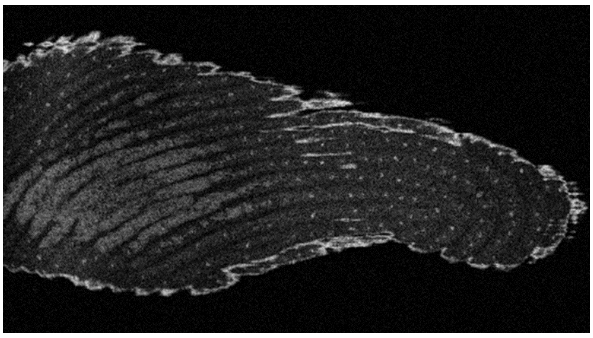

Fig. 7 – En-Face image of the skin

In *Fourier-Domain (FD-OCT)*, the depth information is obtained by calculating the Fourier transform of the spectrally resolved interference fringes in the interferometer detection arm (DREXLER; FUJIMOTO, 2008). FD-OCT has usually two implementations: Spectral-Domain OCT (SD-OCT) and Swept-Source OCT (SS-OCT) also known as optical frequency domain interferometry (OFDI). In SD-OCT, a broad-bandwidth light source is used and the interference spectrum is detected by a spectrometer equipped with a line detector or a camera and in SS-OCT, a high-speed narrow-band tunable light source that sweeps the frequency in time is used (WOJTKOWSKI; SRINIVASAN; KO; FUJIMOTO; KOWALCZYK; DUKER, 2004). The frequency swept light is divided into two beams (sample and reference), that have a time offset that depends on the optical path length difference. As the light frequency is swept in time, the two beams will have a frequency offset and when the beams interfere, a modulation (or beat) is produced. By Fourier transforming this beat frequency signal, depth scanning is obtained.

In Fig.8 the block diagram of the two FD-OCT implementations is presented. In Fig. 8.a, the graph shows the A-Scan (encoded in the signal frequencies within the source bandwidth), obtained through the spectrometer after the Fourier transform, in Fig 8.b the light frequency is swept as a function of time and the Fourier transform is calculated as the frequency is swept. The signals refer to a single point scan in both cases.

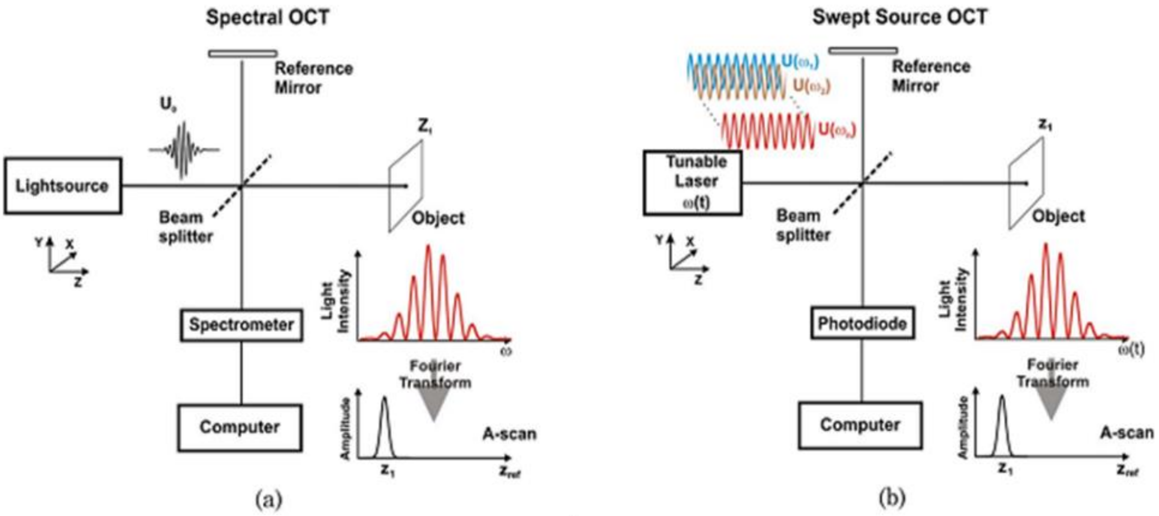

Fig. 8 – Block diagrams of FD-OCT configurations: (a) Spectral Domain OCT; (b) Swept Source OCT. From (WOJTKOWSKI, 2010).

One alternative to a point-scan of Full-field configuration is known Line-Field OCT (YASUNO; MAKITA; ENDO; AOKI; NAKAMURA; YAMANARI; ITOH; YATAGAI, 2005) (YASUNO, ENDO, MAKITA ,AOKI, ITOH,YATAGAI.,2006) that allows the simultaneous depth scanning of an entire line (B-Scan) of the sample at a time, as in Fig.9. In this configuration, a cylindrical lens shapes the light beam into a line that will scan the sample through a rotating mirror controlled by a galvo actuator. The line beam returned from the sample passes through a diffraction grating, where it is dispersed an is focused on a camera where each line represents the wavelength resolved interference of a sample point. In the figure, M is a mirror, CL is a cylindrical lens; L1, L2, L3 and L4 are regular lenses (for the wavelengths of the light source); SLD is a superluminescent diode (the light source), 2D CCD is a CCD camera and a rotating mirror that makes the line beam scan the sample.

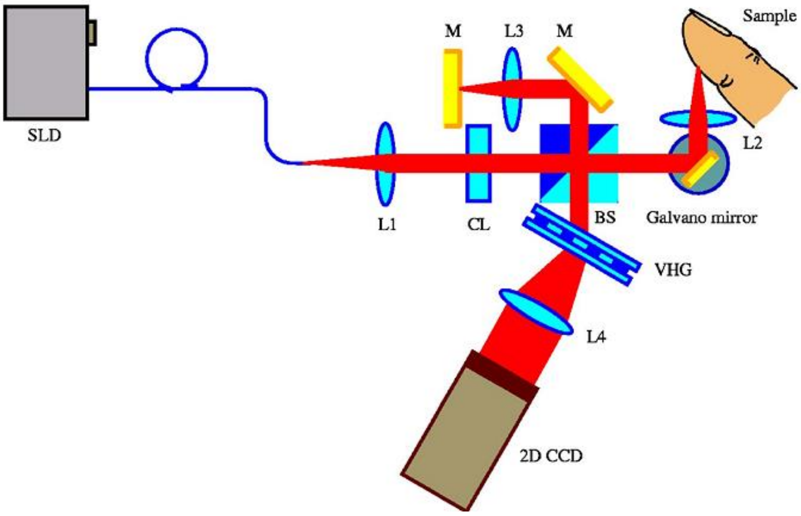

Fig. 9 – Line-field schematics and line scanning on the sample. From (YASUNO, ENDO, MAKITA ,AOKI, ITOH,YATAGAI, 2006)

OCT Design parameters

The choice of an implementation scheme influences important parameters of the system. Resolution, sensitivity, field of view (FOV), penetration depth and scanning speed are essential parameters to a 3D fingerprint acquisition system.

Resolution

Resolution in biomedical imaging is usually defined in terms of the smallest dimension that can be resolved by the optical system, usually measured in microns (μm) and not in dpi (dots per inch) as usual in biometric identification applications. OCT permits obtaining high resolution images, submicron resolutions have been obtained in both time and Fourier domains (DUBOIS; VABRE; BOCCARA; BEAUREPAIRE, 2002), (WOJTKOWSKI; SRINIVASAN; KO; FUJIMOTO; KOWALCZYK; DUKER, 2004) . An interesting feature to mention is that the depth resolution (Cartesian Z-axis) and the lateral (X-Cartesian axis) are dependent on different characteristics (FERCHER, 2010). Depth resolution depends on the wavelength and bandwidth of the light source, being calculated by equation (1):

$$z_{res} = \frac{2.\ln(2)}{\pi}\frac{\lambda^2}{\Delta\lambda} \qquad (1)$$

where λ is the light source wavelength and Δλ is the bandwidth of the light source, both expressed in nanometers (nm).

The lateral (transversal) resolution depends on the focusing properties of the optical beam, determined by the numerical aperture (NA) of the optical system and calculated by the equation (2):

$$t_{res}=\frac{4\lambda}{\pi}.\frac{f}{d} \qquad (2)$$

where λ is the light source wavelength, f is the objective lens focal distance and d is the spot size of the beam on the objective lens, proportional to the numerical aperture of the beam angle of focus (BOUMA, B.E.TEARNEY, 2002) .

Sensitivity

Sensitivity and signal-to-noise ratio (SNR) are used interchangeably in OCT to express the minimum reflected optical power that can be detected, compared to a perfect reflector (FUJIMOTO, 2006). SNR is usually expressed in decibel units (dB). In Table II, the sensitivity equations of TD-OCD, SD-OCT and SS-OCT (WOJTKOWSKI, 2010) are listed for shot noise limited detection. From this table it can be observed that SNR depends of similar most factors (P_o, k_r, k_s,R_s,R_r, e^- and ρ). What makes them different are factors that alter time constants as the electrical bandwidth in TD-OCT or the signal integration time in SD-OCT and the sweep rate in SS-OCT.

Table II – Sensitivity of FD-OCT, SD-OCT and SS-OCT

TD-OCT	SD-OCT	SS-OCT
$\frac{2\rho P_0}{e^{-}\Delta f}.\frac{k_r k_s R_r R_s}{(R_r+R_s)}$	$\frac{\rho P_0 T}{e^{-}}.\frac{k_r k_s R_r R_s}{(R_r+R_s)}$	$\frac{\rho P_0}{2e^{-}.f_{ss}}.\frac{k_r k_s R_r R_s}{(R_r+R_s)}$

where: P_o is the average optical power exiting the interferometer; e- is the electron charge; Δf is the electronic detection bandwidth; k_r and k_s are unidirectional coupling coefficients respectively of the reference and sample arms; R_r and R_s are reflectivity of the reference mirror and the sample respectively; T is the camera integration time; f_{ss} is the sweep frequency of the tunable light source and ρ is calculates by the equation (3).

$$\rho=\frac{e-^{-}\eta}{hc} \qquad (3)$$

where: e- is the electron charge; η is the detector quantum efficiency; h – Planck constant and c the speed of light.

As the electronic bandwidth is determined by the measurement time, that depends on the speed of the optical delay line, it can be expressed by equation (4):

$$\Delta f \cong \frac{2Z_{max}\Delta\lambda}{\lambda_0^2 T} \tag{4}$$

From these equations, a relation between Time-Domain OCT and Fourier Domain OCT can be obtained (5):

$$SNR_{FD-OCT} = \frac{2ln2}{\pi}\frac{Z_{max}}{\Delta z}SNR_{TD-OCT} \tag{5}$$

Where Z_{max} is the axial imaging range and Δz is the axial resolution. For tissue imaging ratio Zmax/ Δz is expected to be very large.

The equation shows that an increase in axial resolution favors SNR_{FD-OCT} in relation to $SNR_{TD-OCT.}$ In theory, FD-OCT systems are capable of having up to 20dB more sensitivity than TD-OCT.

Sensitivities equal or superior to 90dB have been reported in the literature (FERCHER, 2010). For a Line-Field device scanning the human skin, a sensitivity of 75.6dB have been reported (YASUNO, ENDO, MAKITA ,AOKI, ITOH,YATAGAI, 2006). A recent paper reporting a Full Field-OCT imaging system that acquired finger skin images, a sensitivity of 85dB has been reported (AUKSORIUS; BOCCARA, 2015).

Penetration depth

Penetration depth depends on both the source wavelength and the scattering and absorption properties of the sample. The light transmission in biological tissue is mainly limited by water and melanin absorption (FERCHER, 2010). The red and near infrared wavelengths (700 to 1300nm) are preferred as the absorption is minimized in skin, this range is known as the “window of transmission” (GAMBICHLER; MOUSSA; SAND; SAND; HOFFMANN, 2005). OCT skin penetration depths of 1 mm have been reported in (KNUTTEL; BONEV; KNAAK, 2003) and (ZAKHAROV; TALARY; KOLM; CADUFF, 2009), sufficient to scan the epidermis and epidermis-dermis interface (GAMBICHLER; MATIP; MOUSSA; ALTMEYER; HOFFMANN, 2006).

Field of View

The field of view (FOV) is determined by the numerical aperture of the objective lens (and its diameter) used in the OCT, in general low NA allows larger fields of view but the lateral resolution may be affected, a tradeoff between FOV and resolution is usually adopted. As an example the OCT equipment to acquire the 3D fingerprints used in this research a FOV of 14.1mm x 14.1mm (THORLABS, 2016),.

Scanning Speed

OCT technology scanning speeds have improved in recent years, especially in Fourier-Domain schemes. Acquisition speeds of 50,000 A-scans/s have been reported (WOJTKOWSKI, 2010). In finger skin, an acquisition time of 1.6s for a single 2D image of 1.02cm x 1.28cm was obtained (AUKSORIUS; BOCCARA, 2015). A line-field configuration reported an acquisition time of 10s for a volume of 2.1mmx1.4mm x 1.3mm (YASUNO, ENDO, MAKITA ,AOKI, ITOH,YATAGAI, 2006). In the commercial OCT device used in our experiments, speeds near 1/60 images/s (approximately 1 min for image) for a volume of approximately 14.1mm x14.1mm x 1 mm were obtained. This speed was sufficient to obtain acceptable images, although some motion artifacts occurred due to the difficulty to keep the finger still during the acquisition.

OCT Unique Advantages

OCT technology potentially addresses some of the limitations reported in the previous sections such as the following:

- Reconstruction errors: OCT images are not generated by triangulation or profilometry techniques followed by reconstruction, the 3D volumes are natively generated by the equipment. To build 3D fingerprints (point clouds) of the external and internal layers, edge and layer interface detection techniques can be used.
- Contrast problems: OCT does not rely on visible camera images of the finger to obtain images. Layer visibility can be adjusted before acquisition, as a consequence image generation is not affected by contrast and illumination problems
- Variable resolutions: OCT images can provide high depth and lateral resolutions independent of the position of the point in the fingerprints. For newborn babies, a lateral resolution of 5μm (achievable with OCT) would result in 20 points per ridge,

better than minimum required quantity. As the images are collected in 3D, more points per ridge are available.

- Fingerprint Alterations: the access to the internal layers of the skin permits construction of internal (dermal) 3D fingerprints when the skin change is superficial, as detailed in the next sessions.
- Contactless: OCT images are acquired without the need to contact the sensor to acquire images which prevents deformation and facilitates the adoption of technology
- Improved biometric accuracy: the availability of 3D information uncovers rich new information that can be used for improved matching. In addition, some other skin structures such as the sweat ducts and the epidermis-dermis interface can potentially be exploited.

6 – STRUCTURE OF THE FINGER SKIN

The human skin consists of two layers, the dermis and the epidermis. The epidermis can be divided into four sublayers: the *stratum corneum*, the *stratum granulosum*, the *stratum spinosum* and the *stratum basale* (VENUS; WATERMAN; MCNAB, 2010). The deepest layers of the epidermis (*stratum basale*) consists of living cells, which are constantly multiplying and replacing the dead cells from the outermost layer (*stratum corneum)*. Every epidermal cell begins its life in the deepest part of the epidermis and migrates gradually to the *stratum corneum*, suffering a process of hardening as they migrate.

The *stratum corneum*, the outermost layer, is composed of cells that migrate from the *stratum granulosum* and have lost their nuclei and cytoplasmatic organelles. This layer is usually thick on the palms and soles but less thick in other parts of the body. The *stratum granulosum* (granular cell layer) is made of keratin production cells, the keratinocytes. These cells discharge their lipid components in the intercellular space, playing a barrier function and intercellular cohesion within the *stratum corneum*. The *stratum spinosum* is formed by basal cells (from the *stratum basale* layer) that moves to the outer part and form a layer of polyhedral cells connected by desmosomes (a structure that binds cells membranes). The *stratum basale*: thin layer with thickness of one to three cells. Predominance of keratinocytes, although some melanocytes may be up to 5 to 10% of the cell population.

The dermis is a thick and resilient layer that protects the body against injury. It is limited by the interface with the epidermis, an irregular portion made of blunt pegs named dermal papillae (Fig.10), composed of connective tissue. These papillae are arranged in double rows and follows the shape of the epidermal ridges as they mold the epidermis in the fetus formation.

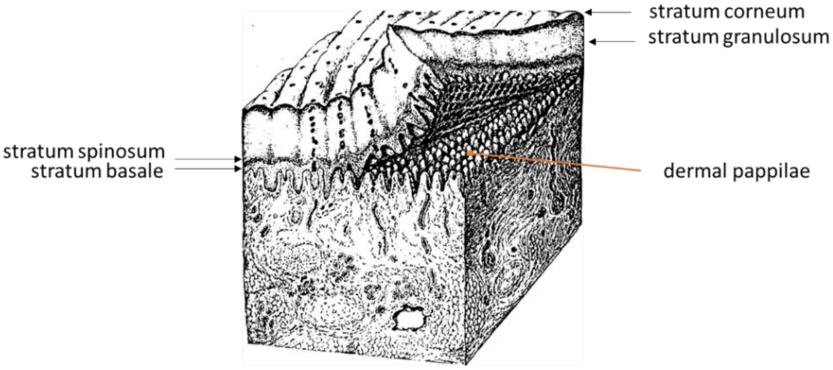

Fig. 10 – Skin layers. From (CUMMINS; MIDLO, 1976)

When the skin is damaged, the original ridge characteristic can be restored if the wound does not reach this level. Burns and caustic agents produce no permanent effect if the papillae level is not damaged.

The skin layer thickness varies in different parts of the body and different people presents different thickness variations in corresponding regions. The epidermis and dermis are of similar thicknesses and the height of dermal papillae is approximately 0.2 mm. In OCT transversal images (B-Scans), the *stratum corneum* and the epidermis-dermis interface are visible as high intensity layers, as shown in Fig.11. Epidermal ridges are developed in the fetus between the third and fourth weeks of the fetal period and no significant alteration occurs in their configuration during the life after birth (i.e. there are permanent). The finger skin capacity of corrugation associated with the moistening by sweat and the absence of hair prevents slipping, for this reason the undulations of the skin are named *friction ridges*.

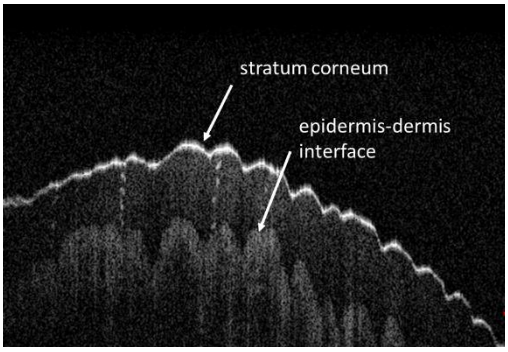

Fig. 11 – B-Scan of the finger skin showing the stratum corneum and the dermis-epidermis interface

Although friction ridges look like smooth lines with constant height and width in 2D fingerprint images, a closer look in OCT images (Fig.12) show that they are irregular, having varied thicknesses and superficial undulations. The sweat pores can be clearly observed as holes on the top of the ridges.

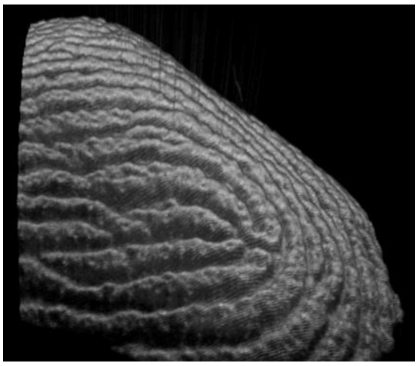

Fig. 12 – Detail of the ridge shapes (rendered 3D OCT image of the finger)

In 2D fingerprints, ridge width varies from 100µm to 300µm, in general the ridge/valley period is approximately 500µm (D.MALTONI, A.JAIN, D.MAIO, 2003). A width difference may exist between the 2D and 3D width measurements since deformation occurs when the ridge is pressed against the 2D fingerprint sensor. This deformation is different in the internal layers of the skin if compared to the external layer (*stratum corneum*), as observed in (GUTIERREZ DA COSTA; MAXEY; SILVA; ELLERBEE, 2014) and is anisotropic (different in each direction). 2D minutiae are features formed by the ridge lines, easily observable in images acquired by a touch-based scanner, as in Fig.13, when ridges form discontinuities as ends or bifurcations. In this case, the parts of the skin that touch the sensor (ridges) are represented in black and the parts that don't touch it are represented by white lines. Minutiae are frequently used in 2D biometric identification.

Fig. 13 – A fingerprint acquired by a touch-based scanner (the yellow circles show an ending and a bifurcation).

In our research, the epidermis layer, especially the *stratum corneum* and the dermis-epidermis interface are the layers of interest to extract the 3D fingerprints as explained in the following session.

7 – IMAGE EXTRACTION AND 3D OCT FINGERPRINT DATABASE

In OCT images (Fig.11), the external part of the epidermis (*stratum corneum*), where the skin contacts the air, appears as a thin bright layer due to a large the refractive index mismatch between the air and the skin, as a consequence the ridges and valleys are clearly visible in these images. Deeper in the skin, the interface between epidermis-dermis has a structure whose shape is very similar to the *stratum corneum* (MIZOKAMI; SILVA; KÜCKELHAUS, 2015) and is visible as a medium intensity section of the skin (if compared to the *stratum corneum*) in the B-scans as the refractive index mismatch is not so large. By detecting the interfaces between the *stratum corneum*/air and the dermis/epidermis, two point clouds, the 3D dermal and 3D epidermal fingerprints can be built (Fig.12). These are named the epidermal and dermal 3D fingerprints.

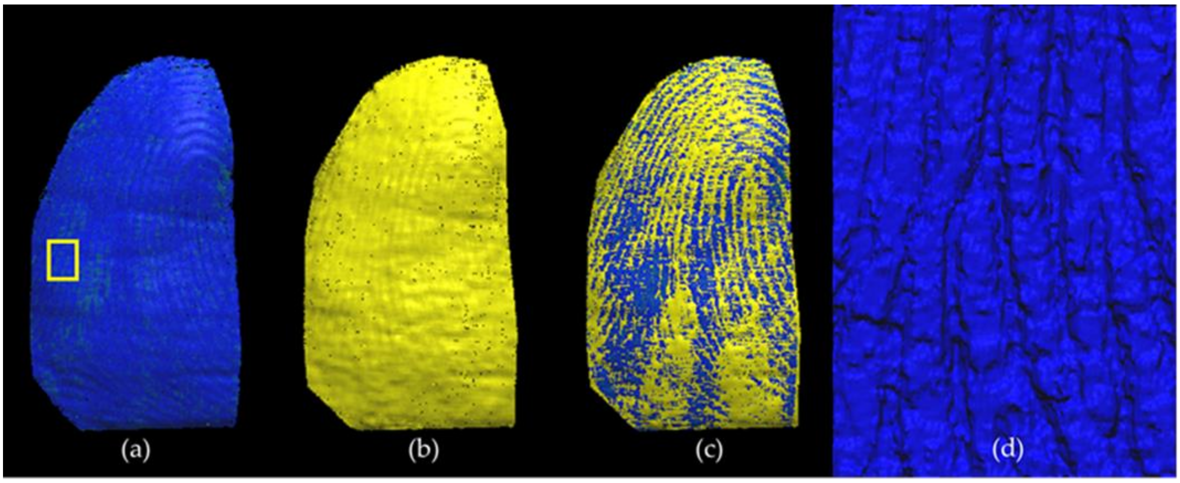

Fig. 14 – 3D fingerprints: (a)3D epidermis fingerprint; (b) 3D dermis fingerprints; (c) 3D registered epidermis and dermis fingerprints;(d) a region around the minutiae (a line ending) known as *minutia cloud* (corresponding to the rectangle in figure (a)).

3D Fingerprint extraction

The OCT acquired images are processed to generate the 3D epidermis fingerprint (external), obtained from the *stratum corneum* and the 3D dermal fingerprint (internal), from the epidermis-dermis interface. Different methods are adopted for each 3D fingerprint. For the epidermis (external), since the *stratum corneum* is a high-intensity sharp line, a Canny edge detector (CANNY, 1986) has been adopted after testing several algorithms such as Sobel, Prewitt, and Roberts (GONZALEZ, RAFAEL C.;WOODS, RICHARD E.;EDDINS, 2004), as it obtained the best results, as shown in Fig.15. The same edge detection processing is executed in two orthogonal directions to increase the amount of points. The stacking of all the detected edges forms the 3D external (epidermal) fingerprint.

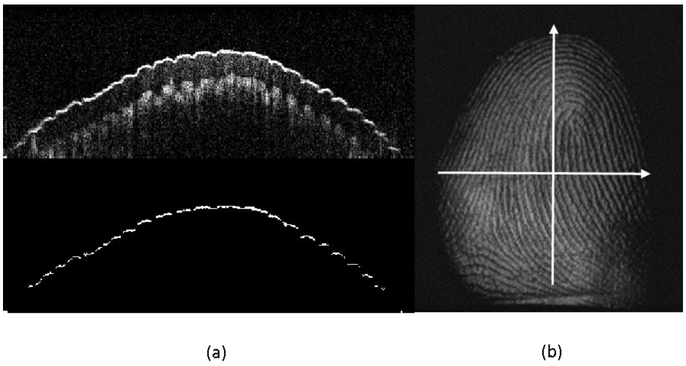

Fig. 15 - Detection of external fingerprint: (a) Original (top) and detected external layer (bottom); (b) detection directions (white arrows).

For computing the internal (dermal) 3D fingerprint, the intensity of dermis-epidermis interface points is first enhanced by the method proposed by (AVANAKI; HOJJATOLESLAMI, 2013) that takes into consideration the intensity contribution of groups of neighbor points in this region. This process results in an enhanced B-scan. Follows the detection of the dermis-epidermis interface by computing for each column of it (A-scan) an intensity profile (plotted in Fig. 16) and detecting the location of points corresponding to intensity peaks, the first corresponding to the *stratum corneum* and the second to the epidermis-dermis interface (used to generate the points of the 3D internal fingerprint). The process is applied to enhanced B-scans obtained from two orthogonal directions as in Fig.16 (i.e. slices along the finger and transversal to it) to increase the point cloud density. The result after the two layer detections are two point clouds, corresponding to the external and internal 3D fingerprints (COSTA; BELLON; SILVA; BOWDEN, 2016).

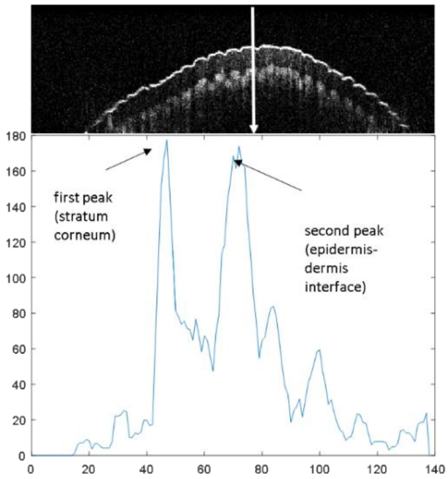

Fig. 16 – Epidermis-dermis detection: (top) A-scan represented by the white arrow; (bottom) the intensity graph of the A-scan

OCT 3D Fingerprint database (OCTDB)

The first 3D fingerprint database (OCTDB) was acquired through a partnership with Stanford University and followed an approved acquisition protocol. 3D images were acquired using a general-purpose OCT device (Telesto OCT System) with a field of view of 14.1 mm X 14.1 mm and a resolution of 7.5µm (equivalent to approximately 1170 ppi). Volumes of 700 x 700 x 256 voxels were obtained from eleven volunteers in two scanning sessions and occurred in different days at the Stanford Biomedical Optics Group laboratory. Each unprocessed image had 245 MB and was reduced 4.3 to 33MB after 3D fingerprint extraction.

The volunteers, whose identity was not linked to the images, had their ten fingers scanned by the OCT device in a 25-minute session. During the acquisition process, no special positioning of the finger, except keeping it relaxed but still during the acquisition were required. The ten fingers were scanned and when needed, additional scans (in the same session) were done if motion artifacts (caused by involuntary motion) were observed. A total of 163 3D fingerprints was obtained (including the external and internal 3D fingerprints from both scanning sessions). During the acquisition, scars, callus, scratching, abrasion and some sweating occurred. Fingers from individuals of both genders were scanned and various types of fingerprint patterns were found in the collection as arches, loops, whorls and twin loops as defined by Galton-Henry (D.MALTONI, A.JAIN, D.MAIO, 2003). During the generation of the 3D images of the OCT database, a few images had low quality problems such as motion artifacts, holes and low density of points, as shown in Fig. 17. Those were not used in the experiments. In addition, 2D images of the fingerprints using a regular contact-based scanner were scanned from the same volunteers.

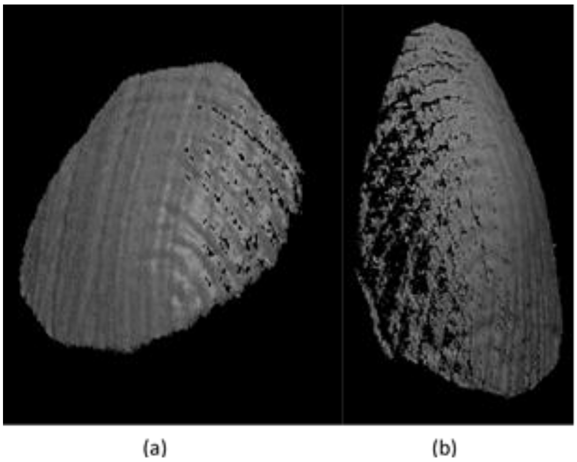

Fig. 17 – Low quality images: (a) Motion artifacts (appear as longitudinal lines in the picture); (b) Holes and low-density regions

The 3D fingerprint images were registered to the X-Y Cartesian plane and saved in XYZ format. The processed images formed the first OCT 3D fingerprint database (OCTDB) to our knowledge. Some samples of OCTDB are presented in Fig.18 (3D) and 19 (2D).

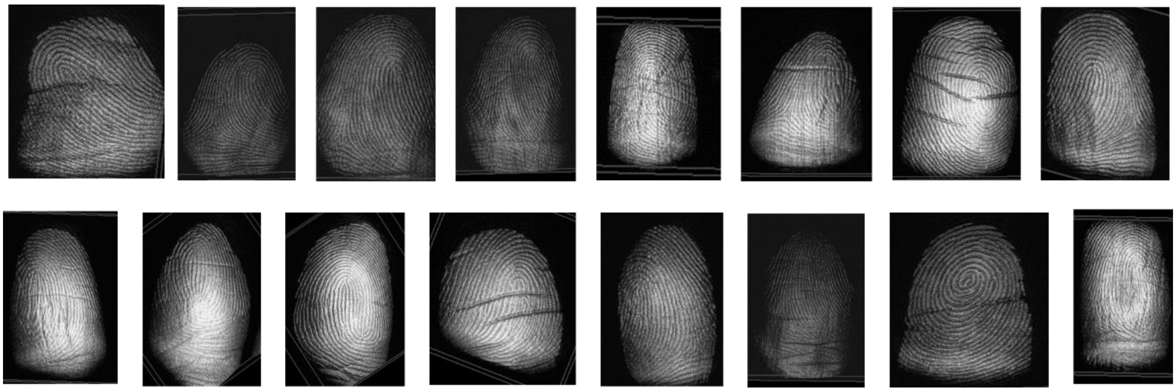

Fig. 18 – Rendered images from the OCT 3D Fingerprint database (OCTDB)

Fig. 19 – 2D fingerprints scanned from the same volunteers (samples)

Additionally, 2D fingerprints of the same volunteers were acquired using a contact-based scanner (Secugen). These fingerprints can be used for comparing matching results of 2D against the 3D methods

This database differs from the others acquired by the other technologies by the higher resolution of images, clearly defined ridges and valleys, accurate scanning of all the skin irregularities and the availability of the internal structures as the sweat ducts and dermal papillae (dermis-epidermis interface). Its use in future research can open the exploitation of new biometric features and innovative matching methods as the one proposed in the next session.

ROI Extraction to Matching

Our proposed matching process uses regions of the 3D cloud around the minutiae, considered distinctive regions of the finger. These were extracted by selecting a frame of 150x150 pixels (X-Y) around the 3D coordinates of the minutiae to obtain the region of interest (ROI), named *minutia cloud*, which is aligned with the XY Cartesian plane. Only two types of minutiae – bifurcations and endings – were used in this experiment since they are the most commonly adopted in identification (D.MALTONI, A.JAIN, D.MAIO, 2003). In Fig. 20, rendered images of two minutiae clouds are shown.

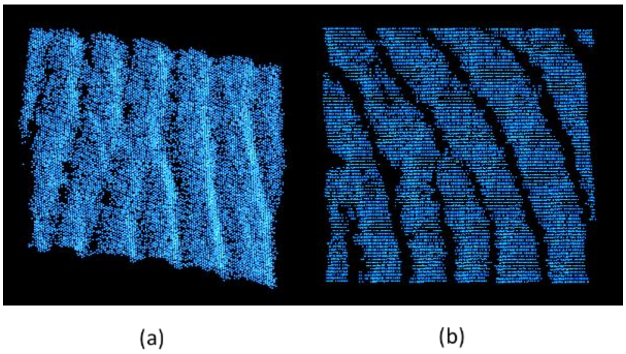

Fig. 20 – Minutiae clouds (rendered images): (a) Bifurcation; (b) Ridge ending.

The minutiae clouds acquired in the first scanning session were stored in a group named *gallery* and the ones acquired in the second session in a group named *probe*. The probe group simulates the enrolled minutiae clouds of a user to be identified by searching the minutiae clouds stored in the *gallery*. The same grouping criteria (*gallery* and *probe*) was adopted to the internal (epidermal) point clouds.

Minutiae clouds are convenient to matching for the following reasons: their configuration makes them very distinctive from mere ridges; they are found in reasonable amounts in the fingers, allowing a direct comparison with the 2D minutiae-based matching methods and they reduce the computational effort to calculate our distinctive features, the KH-maps, obtained from the Gaussian and Mean curvatures of point clouds, to be explained in the next session.

KH Maps

KH maps (Fig. 21) are obtained from the minutiae cloud by the following steps: (1) Gaussian smoothing; (2) interpolation of the 3D points in a regular grid by a 3D linear interpolation; (3) computing curvature values for each 3D point; and (4) converting the curvature values to the KH map. The regular grid is based on the useful area of the 3D minutia cloud. Finally, the regions are segmented by curvature type and different greyscale intensities (greyscale values of 10, 30, 70 and 90 to fit in 7 bits and provide separation of classes by at least 20 intensity levels) are attributed to the curvature types of each minutiae cloud segment for visualization, showing that different segments have clear separation edges. The KH-maps are pre-classified according to the finger type (LP-left pinky, LM-left middle, LR-left ring, LI – left index, LT – left thumb, RP-right pinky, RR-right ring, RM-right middle, RI-right index, RT- right thumb) to reduce the search space.

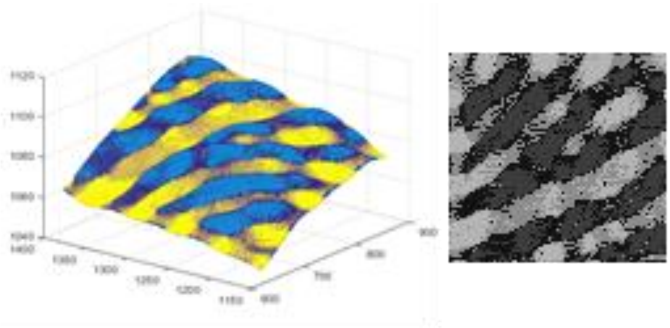

(a) (b)

Fig. 21 - KH map: (a) 3D plotting. Colors correspond to different curvature types (light blue-peak, dark blue-saddle ridge, yellow-pit and orange-saddle valley) and (b) 2D representation

In Fig.22, KH maps obtained from bifurcation and ending regions, the minutiae used in the proposed method are presented.

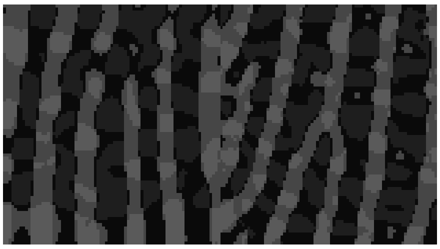
(a) (b)

Fig. 22 – KH maps of: (a) line ending; (b) bifurcation

Other patterns as cores and deltas can be extracted from 3D fingerprints resulting in more complex KH maps (Fig.23). Their extraction from selected regions of the hand could help improve identification although they usually demand larger areas and more computational effort. Their use will be studied in future works.

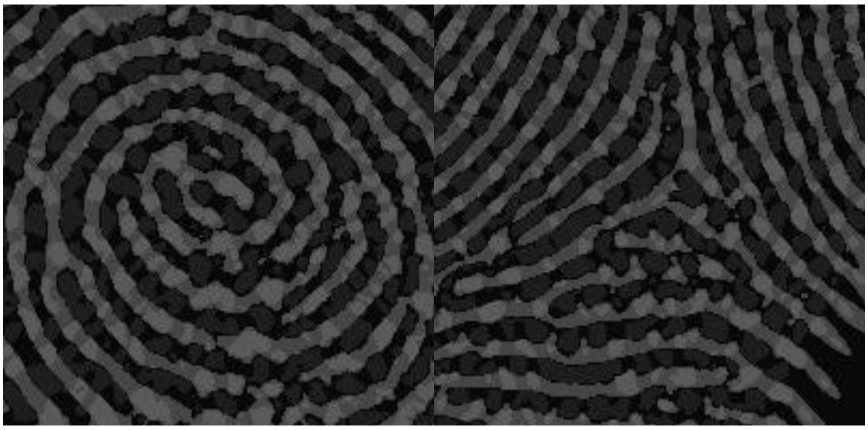
(a) (b)

Fig. 23 – KH maps extracted from: (a) core; (b) delta

8 – 3D FINGERPRINT MATCHING

Our two-step 3D fingerprint matching method starts by extracting the Region-Of-Interest (ROI), i.e. minutiae clouds, from the full 3D fingerprint image. Follows the computation of the KH maps and their LGPs and the final score calculation. Two sets of KH maps are used:1) the *gallery*, resulting from the 3D fingerprints scanned in the first session, simulating the enrollment stage and the 2) *probe*, composed of the 3D fingerprints scanned in the second session, representing the case of a user having its 3D fingerprints scanned to identification. The samples of the *probe* KH-maps are matched against the *gallery* ones. Fig. 24 shows an overview of the matching process. Details are presented in the following subsections.

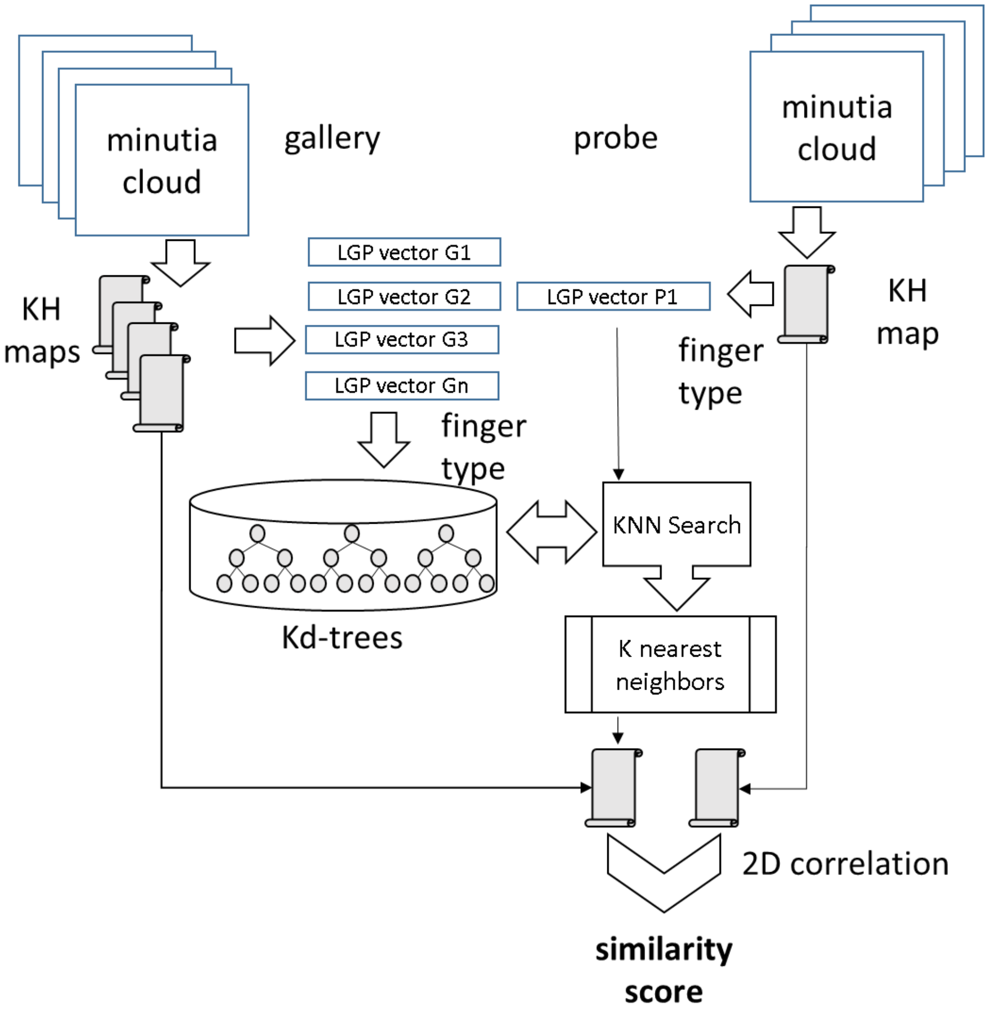

Fig. 24 – Matching method overview

A process to locate and extract the minutiae clouds was devised by first extracting the KH-map of the whole finger (as in Fig.25) and running a minutiae location software (in our case mindtct, an application from NIST Biometric Image Software package that provides the XY coordinates of the minutiae (NIST, 2015). Then the points within a Δx, Δy window (in our case, 150 by 150 pixels) around the minutiae (minutiae clouds) were extracted and saved using the following name convention shown in the Table III. Follows the computation of the KH maps.

Table III – File name convention used for the extracted minutiae clouds

Scanning session	Fingerprint type	X coord.	Y coord.

Fig. 25 - Examples KH-maps of the entire fingerprint

The first step of our method uses Local Gradient Patterns (LGP) (LUBING; HAN, 2012) followed by a similarity calculation (second step) through normalized cross-correlation of the KH-maps. LGP have been successfully used as a texture descriptor for face recognition, allowing discrimination between face and non-face regions based on the image texture (JUN; KIM, 2012)(KANG, 2015).

The Local Gradient Patterns of the KH maps are obtained for each point of the minutia cloud by first calculating the intensity gradient g_i of it to its *p* closest neighbors (in absolute value), then obtaining the average of these gradients, $\bar{g}$ and then attributing a value Si (0 or 1) corresponding to each neighbor, according to the following formula (6):

$$\boxed{s_i = 0 \text{ if } g_i > \bar{g}\text{, 1 otherwise}} \qquad (6)$$

where i=0 to 7

The values of S_i are concatenated to form the LGP value for each pixel, a p-bits number (Fig. 26).

$LGP_i = \Sigma_{i=0}^{7}\{s_i . 2^n\}$, i=0 to 7

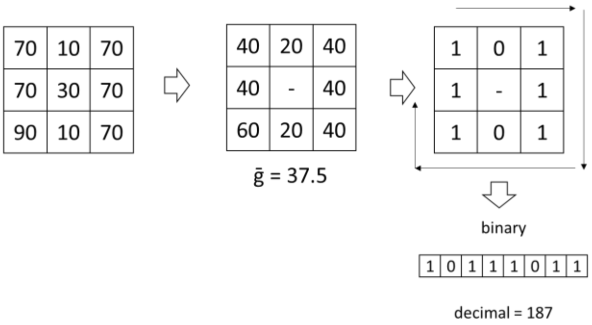

Fig. 26 – LGP calculation, from original intensity values to the final code (8 bits and decimal)

The image is then divided in sections (25 sections in our case) and the histogram of LGP values for each section is calculated and concatenated to form a representative vector used for the first classification step. The LGP vectors, calculated for each gallery KH map, are used to build ten Kd-Trees (BENTLEY, 1975), using the LGP vector as the key and specifying the Euclidean distance as the distance metric, to speed-up k-Nearest Neighbor searches (KNN) . One Kd-Tree for each finger type (pinky, ring, medium, index and thumb from left and right hands) was built. The probe minutiae cloud has its KH map calculated, its finger type determined and LGP descriptor built. Then a KNN search on the Kd-Tree corresponding to that finger returns the K closest neighbors using Euclidean distance. Finally, the 2D correlation is executed between the probe KH map and all the K closest neighbors to determine the similarity score used for matching.

We applied the normalized cross-correlation as a similarity measure since it provides a measure of the correlation between two images (KARNA; AGARWAL; NIKAM, 2008). This approach has been used previously for template and fingerprint matching (D.MALTONI, A.JAIN, D.MAIO, 2003). In our case it serves two purposes, as a means for registering the KH maps and to measure their similarity. The output of the correlation function is a 2D array, and the maximum value of this array (corresponding to the function maximum) was used as the similarity score. The normalized cross correlation (CORR2D) can be calculated by the equation (7).

$$CORR2D(u,v) = \frac{\Sigma_{x,y}[f(x,y)-f_{u,v}].[t(x-u,y-v)-t_m]}{\left\{\Sigma_{x,y}[f(x,y)-f_{u,v}]^2.[t(x-u,y-v)-t_m]^2\right\}^{0.5}} \qquad (7)$$

Where f(x,y) and t(x,y) are the images being correlated

The minutia cloud matching process is repeated for all the minutiae clouds found in each finger (*probe*) and a score S (matched minutiae cloud divided by the total amount minutiae clouds found in the probe) for all the Rank-1 matches is calculated. The FARxFRR (False Acceptance Rate x False Rejection Rate), CMC (Cumulative Matching Characteristic) and ROC (Receiver Operator Characteristic) curves were plotted based on the S score to evaluate the accuracy of the method. Other descriptors were tested in our research as local binary patterns (ZHAO; PIETIKAINEN, 2007), local gradient increasing pattern (LUBING; HAN, 2012) but LGP achieved the best matching results.

Average execution times are 1.0735s for building the Kd-Tree (whole OCTDB database) and 0.0072s for the CORR2D calculation.

9 - EXPERIMENTS AND MATCHING RESULTS

We measured the matching accuracy of our matching method using two databases, the OCTDB and a public database. In addition, we evaluate the compatibility of the minutiae clouds extracted from the dermis and epidermis to check if dermis 3D fingerprint can be used when the epidermis is altered or damaged.

3D Fingerprint Images Database from Hong Kong Polytechnic POLYUDB

A public database gently made available by the Hong Kong Polytechnic University, named “The Hong Kong Polytechnic University 3D Fingerprint Images Database” (KUMAR, 2013), referred as POLYUDB in this work, was used to test the matching method applicability and allow a comparison with OCTDB matching. This database has around 1,560 3D images from 260 subjects, around six images from same finger per each subject, plus seven 2D images that were used to generate the 3D images. In our work we selected 88 3D images from 44 subjects, the ones that allowed the best calculation of the curvature types. Those had clear definition of curvature types as opposed to images excessively smoothed and containing artifacts, where the curvature type segments were not distinguishable, as shown in Fig. 27. Just as a comparison, in (KUMAR; KWONG, 2013) , just used a subset of POLYUDB with 135 subjects was used.

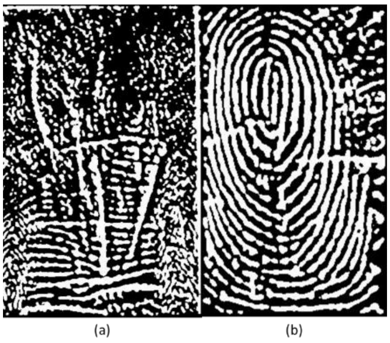

Fig.27 – Black and white representation of entire fingerprint KH maps: (a) bad quality image with ridges unclear and noise; (b) acceptable quality image

Some differences between the OCTDB and the POLYUDB were observed, the ridge heights and valley depths in the first (OCTDB) are bigger than in the second, suggesting that some smoothing was applied to the POLYUDB. The OCTDB finger images are more irregular reflecting the nature of the finger skin as opposed to a shape approximation in the case of POLYUDB. Another significant difference from the POLYUDB is that the amount of points per area used in the reconstruction is higher, making it denser and more regular that the OCTDB. Finally, in POLYUDB the entire fingerprint area is covered what is not the case in the OCTDB database, where areas of 14.1 mm x 14.1mm were acquired. For the POLYUDB matching, the pre-classification based on the finger type could not be used since the finger type information was not available. A single Kd-tree was built to the search.

KH Map Matching (CORR2D)

A test with KH maps from different fingers (and users) was executed to evaluate the accuracy of the method by first trying to match a single minutia cloud from the *probe* to the ones in the *gallery* to evaluate how accurate the use of a single minutiae cloud was for identifying a finger. Then matching was applied using whole set of minutiae found for each the finger of the *probe* to the *gallery* to measure the increase in matching accuracy.

It has been observed that the CORR2D scores drops if the images were misaligned. For this reason, an additional pre-alignment of the KH maps was computed before calculating the score. During the KH map matching tests, it has been observed that the window size influenced the CORR2D index values (in the range [0, 1]), small areas frequently presented false high similarity values. After tests with window sizes varying from 20x20 to 200 x 200, it has been determined that, an area of 100x100 pixels maximizes the CORR2D index.

Tests with the OCTDB Database

Tests using 3,945 minutiae clouds extracted from 163 3D fingerprints (epidermal and dermal) of ten volunteers (in two scanning sessions) were executed to evaluate the matching accuracy. The minutia distribution is shown in Fig.28, on average 4.12 minutiae clouds per finger were found.

The first test aims to evaluate if a single minutia from the probe could be identified in the gallery. The resulting FARxFRR and CMC curves, are shown in Fig. 29.a. An EER (equal error rate) of 12.77% and an identification rate of 75% for Rank-1 (being Rank-k the k matches with highest score, in decreasing order) using the same threshold (of EER) was obtained. The second test evaluated the accuracy of the method to match a finger using all the minutiae clouds found in a finger (from *probe*). 86 fingers from the *probe* were matched. The resulting FARxFRR and CMC curves are shown in Fig. 29.b. An EER of 3.8% was obtained and an identification rate of 94.23%, showing a significant improvement was obtained for Rank-1.

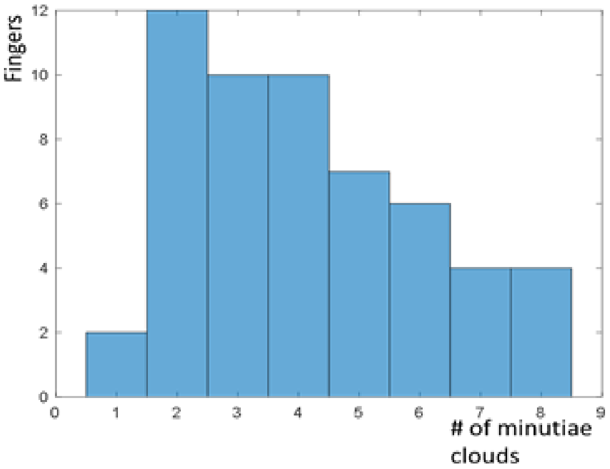

Fig. 28 – Fingers x amount of minutiae for OCTDB

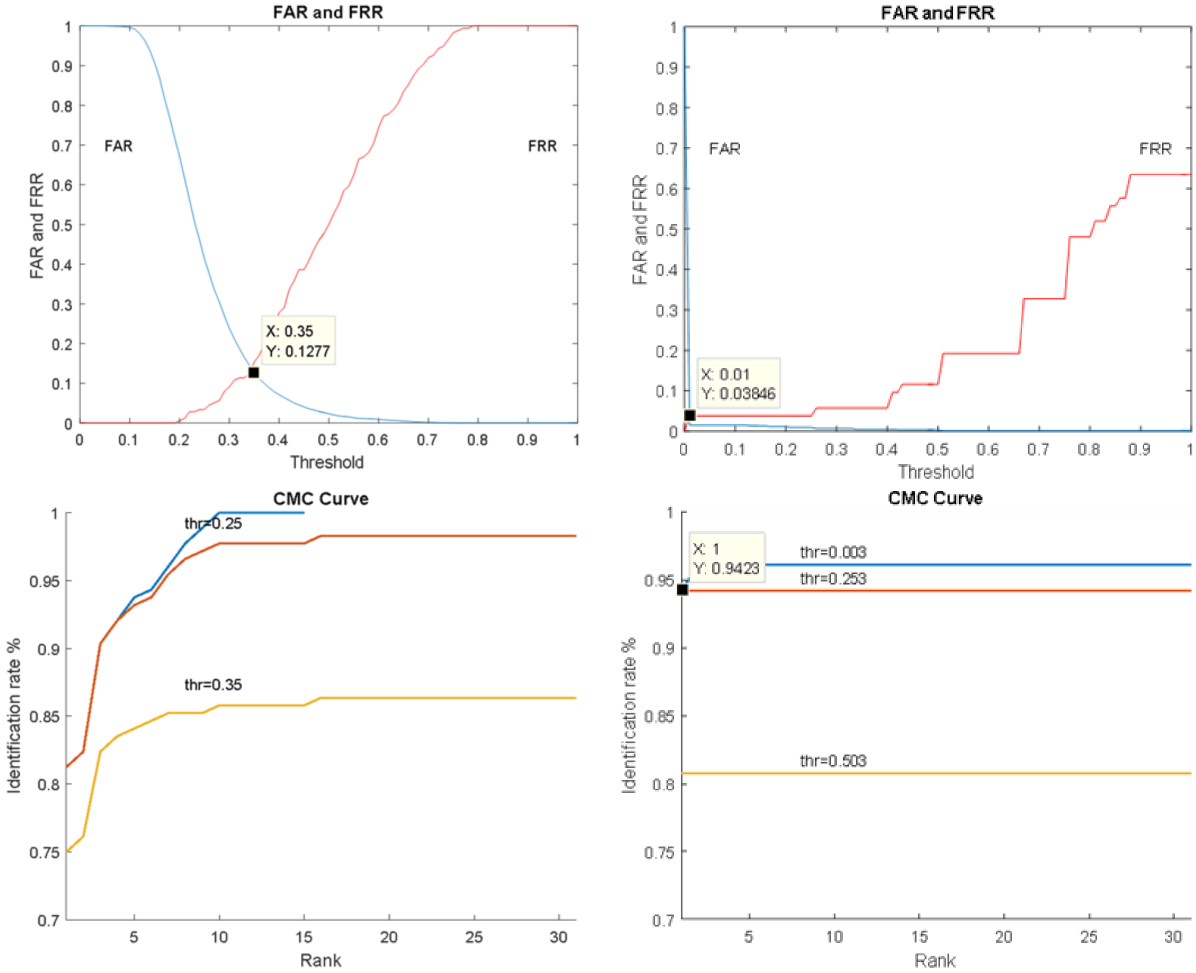

(a) (b)

Fig. 29 – FAXxFRR and CMC curves for matching (OCTDB): (a) single minutia; (b) multiple minutiae

Tests with POLYU database

Tests using 350 minutiae clouds extracted from 86 3D fingerprints of 43 volunteers were executed to evaluate the method accuracy and allow a comparison with the OCTDB database results. An average of 3.97 minutiae clouds per finger was found in the POLYU database with the distribution shown in Fig. 30. As in the previous database tests, single and multiple minutia cloud tests were run. For single minutiae, an EER of 12.36% and a CMC curve with 77.61% recognition rate for the POLYUDB was found (for the EER threshold) as in Fig.31.a. Recognition rates superior to 80% can be obtained if other thresholds are used. For multiple minutiae, a significant improvement was found an EER of 9.96% and an identification rate 99% for Rank-1 was obtained (Fig.31.b). A comparison of the EER and identification rates obtained for the OCTDB and POLYUDB show that the obtained EER and identification rates are similar, as detailed in Table IV.

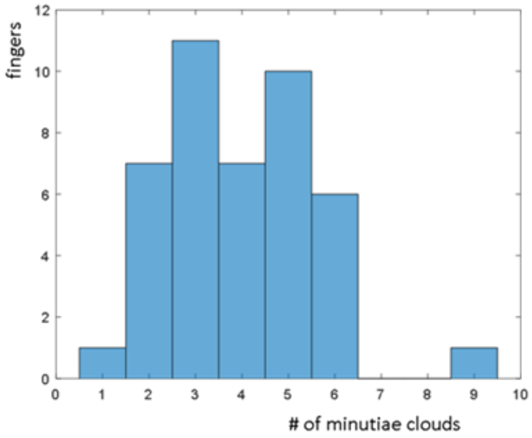

Fig.30 - Fingers x amount of minutiae for POLYUDB

TABLE IV - Results for OCTDB and POLYUDB

	OCTDB	POLYUDB
EER (one minutia)	12.77%	12.36%
Ident. Rate (one minutia)	75%	77.61%
EER (mult. minutiae)	3.8%	9.96%
Ident. Rate (mult.minutia)	94.23%	99%

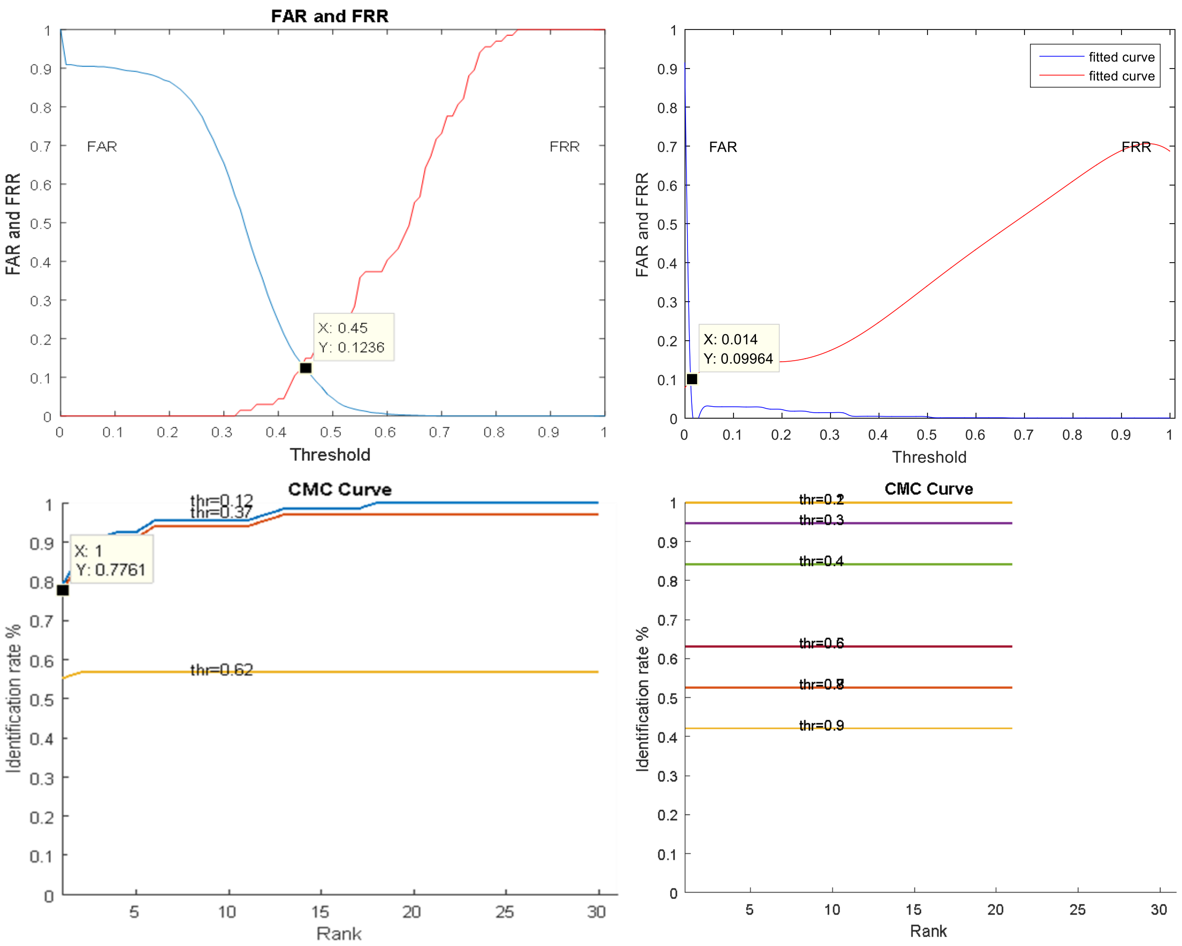

Fig. 31 – FARxFRR and CMC for finger matching with multiple minutiae (POLYUDB)

Comparison with 2D matching results

A matching test, using 2D fingerprints scanned from the same volunteers of OCTDB was executed. NIST bozorth3 matcher (NIST, 2015) was used to obtain the matching scores for this 2D fingerprint set. An EER of 5% and an identification rate of 93.2% (Fig.32) were obtained. In Table V the comparison with the 3D matching is presented showing favorable results to 3D matching.

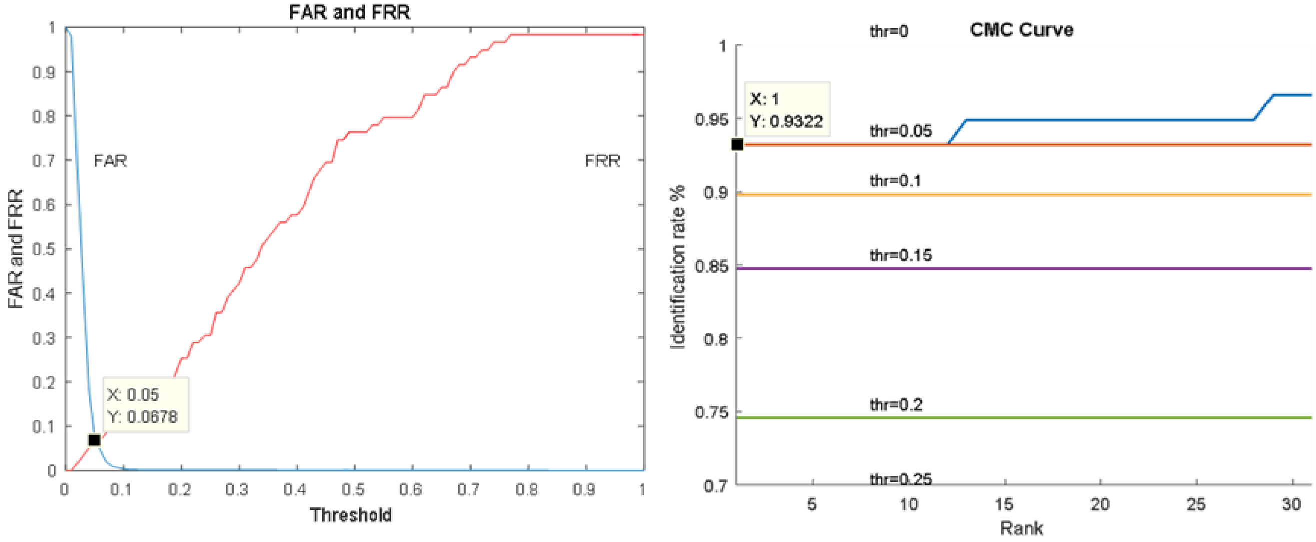

Fig. 32 – FARxFRR and CMC curves for 2D matching

TABLE V - Results for OCTDB: 3D and 2D

	3D	2D
EER	3.8%	5%
Identification Rate	94.23%	93.2%

Compatibility of 3D Dermal and Epidermal Fingerprints

The hypothesis that the dermal 3D fingerprints can be used for matching when the epidermal fingerprint due to their significant similarity (Fig. 33) is tested. Images from 3D epidermis x dermis fingerprints from the gallery and probe sets were selected to the matching test. The amount of 3D image pairs used in this test was smaller than in the Epidermis x Epidermis test, because only images with high contrast and low noise level were used, selected through visual inspection, a total of 11 fingers from 5 volunteers and a total of 52 minutiae clouds. As the structure of the internal and external fingerprints are compatible (MIZOKAMI; SILVA; KÜCKELHAUS, 2015), the degree of similarity of the KH maps of the dermis and epidermis is expected to be high as their correspondent matching scores.

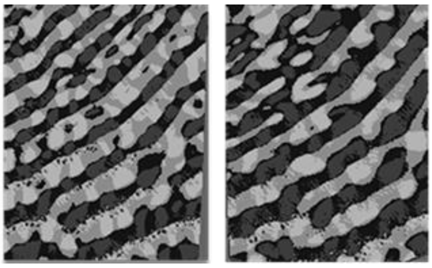

Fig. 33 – Curvature maps of the external (left) and internal (right) fingerprints

As can be seen in Fig. 34, the resulting FARxFRR and CMC curves show an EER of 0.6% and an identification rate of 88.89% (rank 1) when a threshold of 0.006 is used. The identification rate obtained using the dermis is typically inferior to regular 2D due to the smaller percentage of minutiae coincidence between the epidermis and dermis, as reported in (MIZOKAMI; SILVA; KÜCKELHAUS, 2015). However, the identification rate obtained was superior to the results obtained by the traditional invasive process used in identification of corpses, (exposure of the dermis by chemical process) as (MIZOKAMI; SILVA; KÜCKELHAUS, 2015).

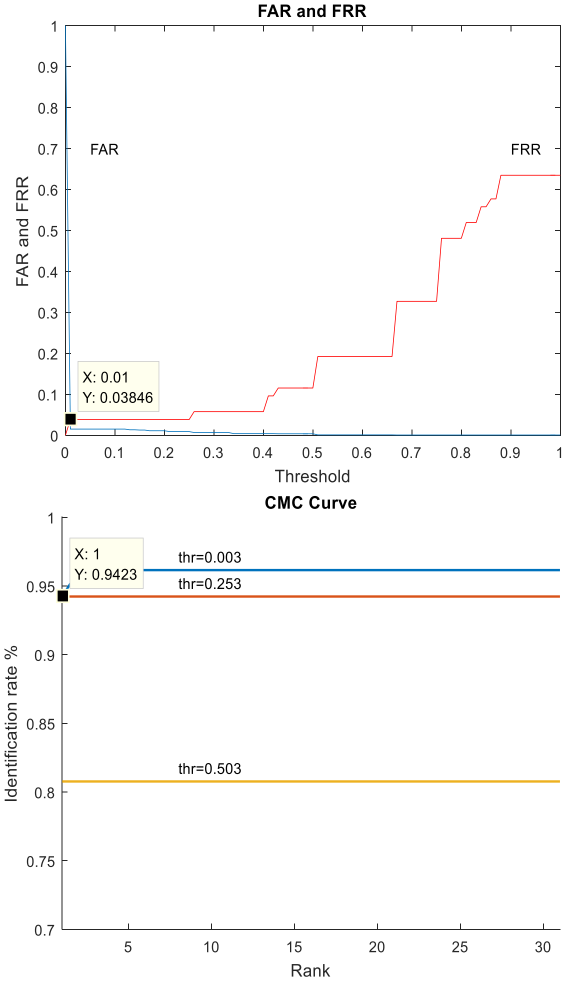

Fig. 34 – FARxFRR (top) and CMC (bottom) for epidermis KH maps

Unrolled 2D fingerprints comparison

An additional test with unwrapped 2D fingerprints obtained from 3D clouds through a based on the described in (JAIN; ABRAMOVICH, 2011) and (CHEN; PARZIALE; DIAZ-SANTANA; JAIN, 2006) was executed to assess the compatibility of the 2D fingerprints obtained from the OCT images. The method uses a parametric approach to obtain the unrolled fingerprint and starts with the registration of the 3D fingerprint to the Z Cartesian axis as shown in Fig. 35. It can be observed that the 3D fingerprint is aligned with Z-axis at -45° with the X and Y axis and all the point cloud (x,y,z) coordinates are positive. After that, starting from the z=0 coordinate, the points at transversal planes parallel (slices at height z_i) to the X-Y Cartesian plane are selected and curve fitting is applied to find the circle that best fits the cloud points at that height (z), as in the dashed semi-circles in Fig. 35. The fitting results in the center position (C) and a radius (R). Having this information, the difference between the radius and the distance of each cloud point to C, named point radius (d) is calculated as shown in the plot (Fig.35). The maximums and minimums of this plot are calculated, these correspond to the position of ridge tops and the valley bottoms. Each point of the ridge in that plane (slice at height z_i) is then mapped to a line segment. The Cartesian coordinates are converted to polar coordinates (ρi,Θi) and the arc length in relation to a plane at 45° with the X and Y axes corresponds to the o a linear position in the dashed line shown in Fig.36. The point intensity varies from 0 to 255 (in greyscale) depending on the proximity of a maximum or a minimum, assuming a sinusoidal intensity variation between them, resulting in the pattern depicted by the vertical line in Fig. 36.a. The images of the lines (zi) are stacked to form the unrolled fingerprint that is converted to black and white for matching as in Fig. 36b.

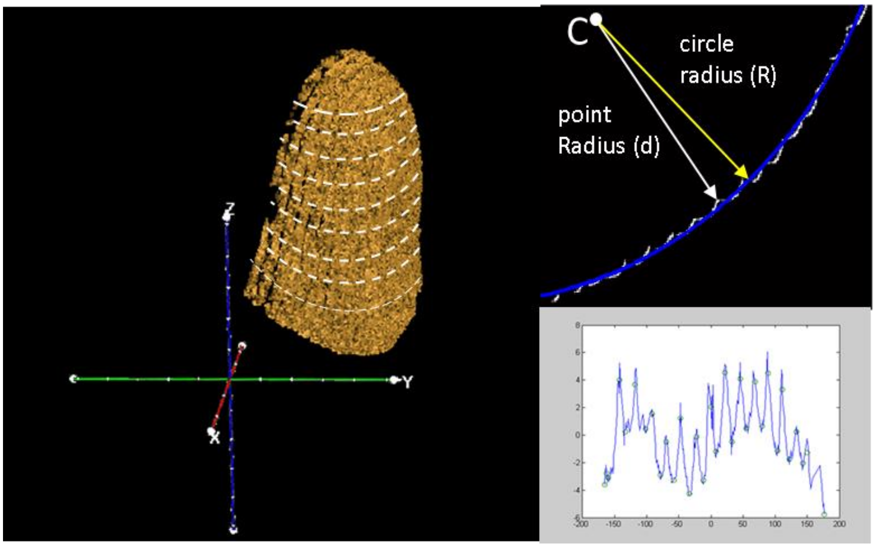

Fig. 35 – 3D Fingerprint aligned with the Z axis: (a) perspective view; (b) top view

A 2D test database, named COMPDB (compatibility database) has 180 images and is composed of: ten 2D regular fingerprints scanned using a 500 ppi contact-based optical scanner plus a database obtained from the Fingerprint Verification Competition 2000 (database DB3) with images scanned with an optical scanner and the same resolution ("FVC2004: the Third International Fingerprint Verification Competition", 2003). The "unrolled" fingerprints (Fig. 36) were converted to a 500 dpi black and white image and matched using the demo version of the Verifinger software, downloaded from (NEUROTECHNOLOGY, 2016).

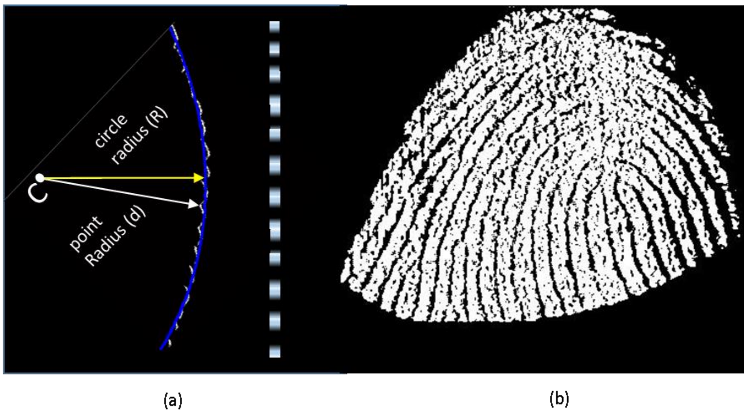

Fig. 36 – Mapping of clouds points at height z to: (a) linear representation ;(b) the resulting unrolled fingerprint

Four flat fingerprints (Fig.37) were generated by selecting the images that resulted in the best finger-to-valley contrast. These unrolled fingerprints were tested against the COMPDB database. The Verifinger demo application was configured to a FAR from 0.1% to 0.001% to cover most of the practical scenarios.

The results, shown in Table VI show that the finger-prints were correctly matched against regular 2D fingerprints (scanned by a contact-based scanner) for different false acceptance rates (0.1%, 0.01% and 0.01% configurable in the software), in all except one case where the unrolled image has noise as marked in the "positive" cases where the matched fingerprint was the correct one.

Fig. 37 - Examples of unrolled fingerprints (top) and their correspondent regular fingerprints(bottom), scanned with a regular fingerprint scanner. (a) left ring, (b) left middle, (c) left ring and (d) left pinky.

Table VI - UNROLLED FINGERPRINT COMPATIBILITY

FAR	0.1%	0.01%	0.001%
Left Index	Positive	Positive	Negative
Left Middle	Positive	Positive	Positive
Left Ring	Positive	Positive	Positive
Left Pinky	Positive	Positive	Positive

10 - QUALITY MEASUREMENTS

During the matching tests it has been observed a large overlap of match and no-match score ranges for the results obtained, as can be seen in Fig. 38, where the match and no-match score distributions for OCTDB (COR2D matching scores) are presented. As the database of minutiae clouds is larger than the amount of correspondent ones, the amount of matches is smaller than no-matches.

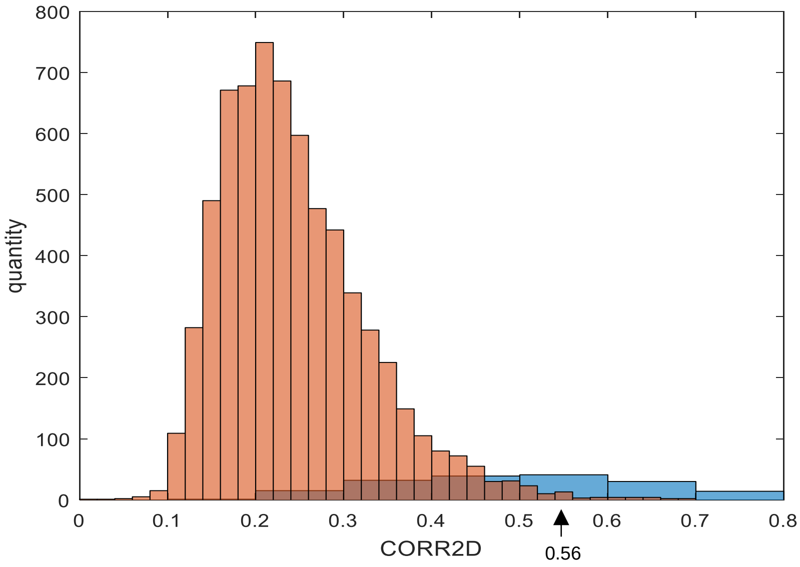

Fig. 38 – Matching scores distribution (CORR2D). Match (blue), No-match (red). The arrow indicates the threshold to eliminate the uncertain no-matches

One of the possible reasons for having unexpected low score matchings (in true cases) is the presence of holes or regions of low density if compared the average of the minutiae cloud. Another reason would be noise, which can cause sharp transitions may lead to spurious curvature values, as can be seen in Fig. 39.

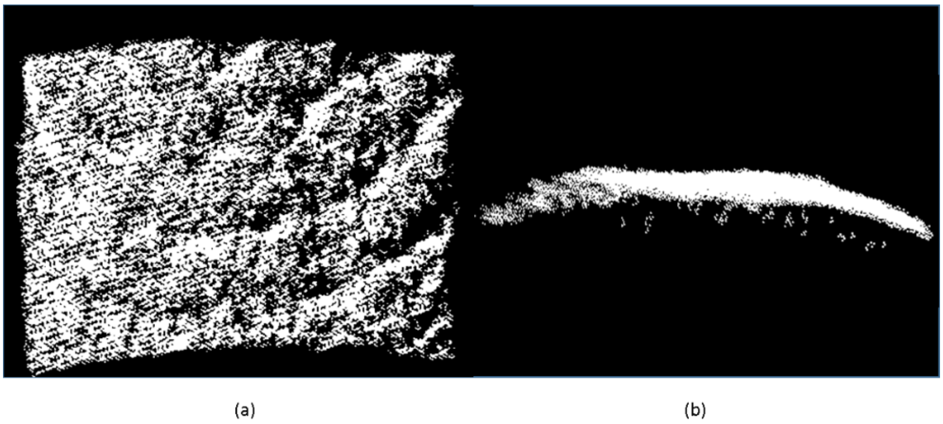
(a)
(b)

Fig. 39 – Quality problems. (a) holes; (b) noise.

The ranges (Table VII) separate the regions where the no-match or match is certain (no overlap between match and non-match) or uncertain (overlap between match and no-match). From the graph, a threshold of 0.56 for COR2D was considered satisfactory to eliminate the uncertain no-matches for the OCTDB database as only 23 misclassifications out of 6,810 occur

Table VII – Matching scores ranges (OCTDB)

Database	No-Match	Uncertain	Match
OCTDB	0 to 0.2	0.2 to 0.66	0.66 to 1

Image quality evaluations can prevent matching inaccuracies, in (KUMAR; KWONG, 2013) a 2D quality criteria, was evaluated to check if the quality of 2D images (used in the triangulation process) could be a predictor of the quality of 3D point clouds but the approach was not effective in predicting the matching performance. In (KUMAR; KWONG, 2015), the need quality evaluation of the 3D reconstruction was suggested as a future research direction but no suggested measure was presented. Quality indicators that could help pre-evaluate the images before the matching calculations can minimize the computational cost and serve as a feedback during the acquisition process to improve the collected images through re-acquisition.

Three quality indicators related to the reported problems (noise and holes) were proposed: local density (LDENSITY) and two smoothness measurements proposed by (BESL, 1988), ρ1 and ρ2. Their effectiveness in helping separate the match and no-match minutiae clouds were evaluated.

The local density is calculated by dividing the amount of pixels in the minutiae cloud by the area X-Y, measured in square pixels as in equation (8).

$$\text{density} = \frac{N\ of\ pixels}{area} \tag{8}$$

where the *area* is measured in square pixels

The density indicator of two minutiae clouds being matched is calculated by dividing the density of one minutiae cloud (density1) by the other (density2), as in equation (9).

$$dens = \frac{density1}{density2} \tag{9}$$

The smoothness indicator is calculated by fitting a plane to each point of the minutia cloud and its 9x9 neighbors and calculating the planar RMS (root mean square) fit error of the whole minutia cloud to the plane. The RMS is divided by the total amount of points of the minutia cloud, as in the equations (10) and (11).

$$\rho_1 = \left(\frac{1}{|I'|}\sum_{(x,y)\in I'} \varepsilon_{1,3}(x,y)\right) \qquad (10)$$

$$\rho_3 = \left(\frac{1}{|I'|}\sum_{(x,y)\in I'} \varepsilon_{1,3}^{3}(x,y)\right)^{1/3} \qquad (11)$$

where I´ is the amount of image pixels (excluded the ones in image edges) and $\varepsilon_{1,3}$ (x, y) is the planar RMS fit error for the 3x3 window at the pixel (x, y)

During the tests, it was noticed with the ρ_1 and ρ_3 indicators, a higher absolute value was associated to increase in the RMS plane fitting error. For this reason, it was decided to work with the inverse of these indicators ($1/\rho_1$ and $1/\rho_3$) as the quality criteria. The average of the two quality scores of the minutiae clouds being matched was used to obtain the evaluation graphs.

Quality Measurements for OCTDB

The distribution scores to the proposed quality indicators for OCTDB is presented in Fig. 40 and Fig. 41. It can be noticed that $1/\rho_1$ and $1/\rho_3$ have similar distributions but different from *dens.*

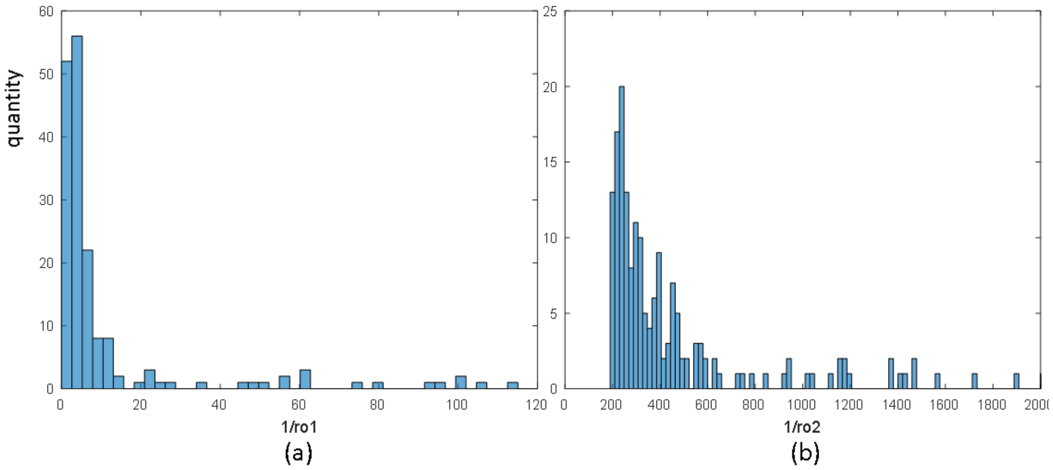

(a)

(b)

Fig. 40 – Quality indicators for OCTDB: (1) 1/ρ1; (b) 1/ρ3

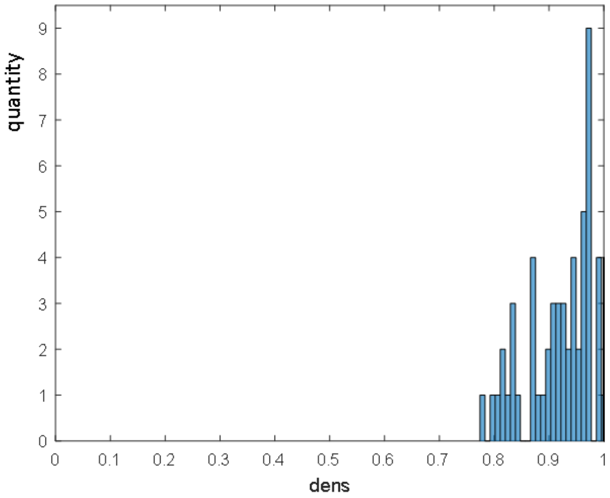

Fig. 41 – Quality indicator for OCTDB: dens

Since different normalization schemes can help promoting the separation of classes, as suggested in (ABAZA; HARRISON; BOURLAI, 2012) and (ABAZA; BOURLAI; ROSS; HARRISON, 2014) we tested linear and non-linear (Gaussian) normalization schemes to the quality indicators and generated graphs of match/non-match distributions using as threshold the 0.56 for CORR2D scores that allowed a good tradeoff between “match” and “no-match” scores. The Gaussian normalization tends to attribute to values close to the average of the scores. For ρ1 and ρ3, the best normalization scheme was Gaussian normalization, as promoted better separation of classes as shown in Fig.42.

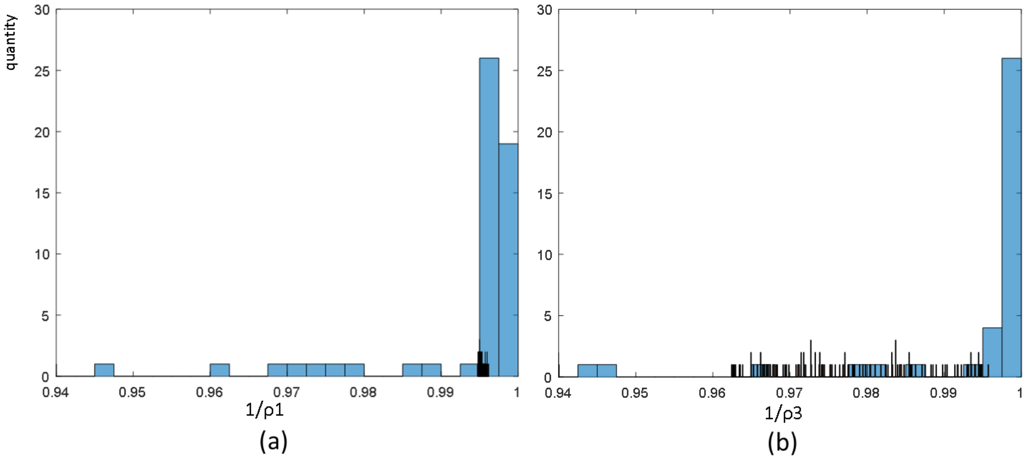

Fig. 42 – Normalized (OCTDB) scores (Gaussian) to: (a) ρ1;(b) ρ3. In blue the “match” scores and in red the “no-match” scores.

It can be observed that, for ρ1, values smaller than 0.9948 and greater 0.9962 tend to be a positive match. For ρ3, with Gaussian normalization, values smaller than 0.9623 and greater than 0.9957 tend to be a positive match. For the *dens* quality indicator, a linear normalization scheme promoted the best separation of classes as shown in Fig. 43. It can be observed that the separation of classes (match/no-match) is not as efficient as in the previous indicators but some amount of scores can be considered a n-match for values greater than 0.526.

Fusion of quality scores was not possible as the normalization schemes were different for the quality indicators.

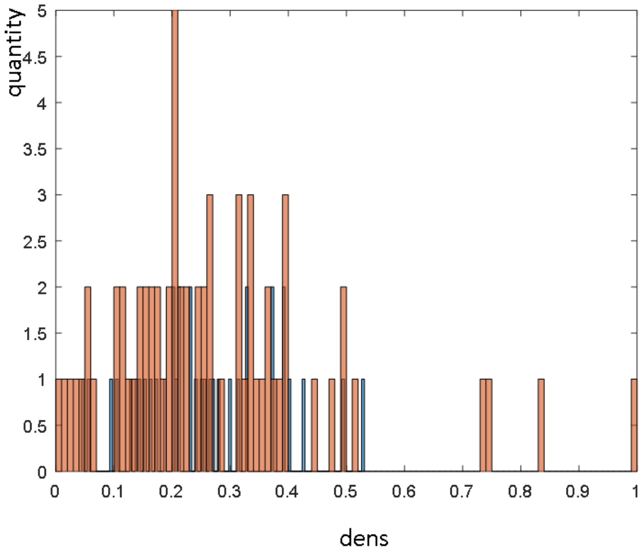

Fig. 43 - Normalized (OCTDB) scores (linear) for dens quality indicator

Quality Measurements in POLYUDB database

The quality indicators ρ1 and ρ3 were applied to the POLYUDB database to test their efficacy in detecting quality problems. The CORR2D score distribution to this database is plotted in Fig.44, a large overlap was also observed. The score range is shown in Table VIII.

Table VIII – Matching scores ranges (POLYUDB)

Database	No-Match	Uncertain	Match
OCTDB	0 to 0.2	0.2 to 0.7	0.7 to 1

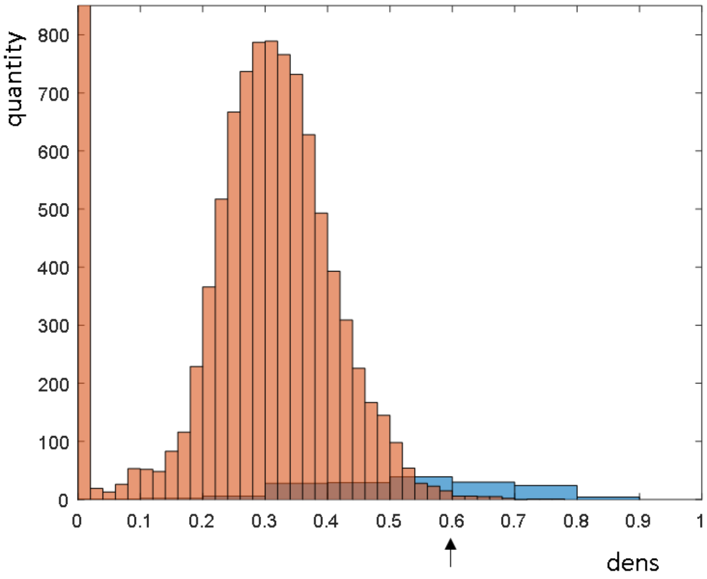

Fig. 44 – CORR2D score distribution to POLUYDB

As the images of POLYU database are significantly smoothed, the $1/\rho_1$ and $1/\rho_3$ are very similar and the quality indicators did not present a good separation of classes for neither the linear nor the Gaussian normalization schemes, as shown in Fig.45. For this reason, the ratio between the ρ_1 and ρ_2 for the two images being matched ρ1/ ρ1’ and ρ2/ ρ2’ was tested. In Fig. 46.a and 46.b it can be noticed that the linearly ratios ρ1/ ρ1’ and ρ2/ ρ2’ promoted a better separation of classes than the Gaussian (for ρ1/ ρ1’ greater than 0.32 and ρ2/ ρ2’ greater than 0.55) but some significant overlap still remains.

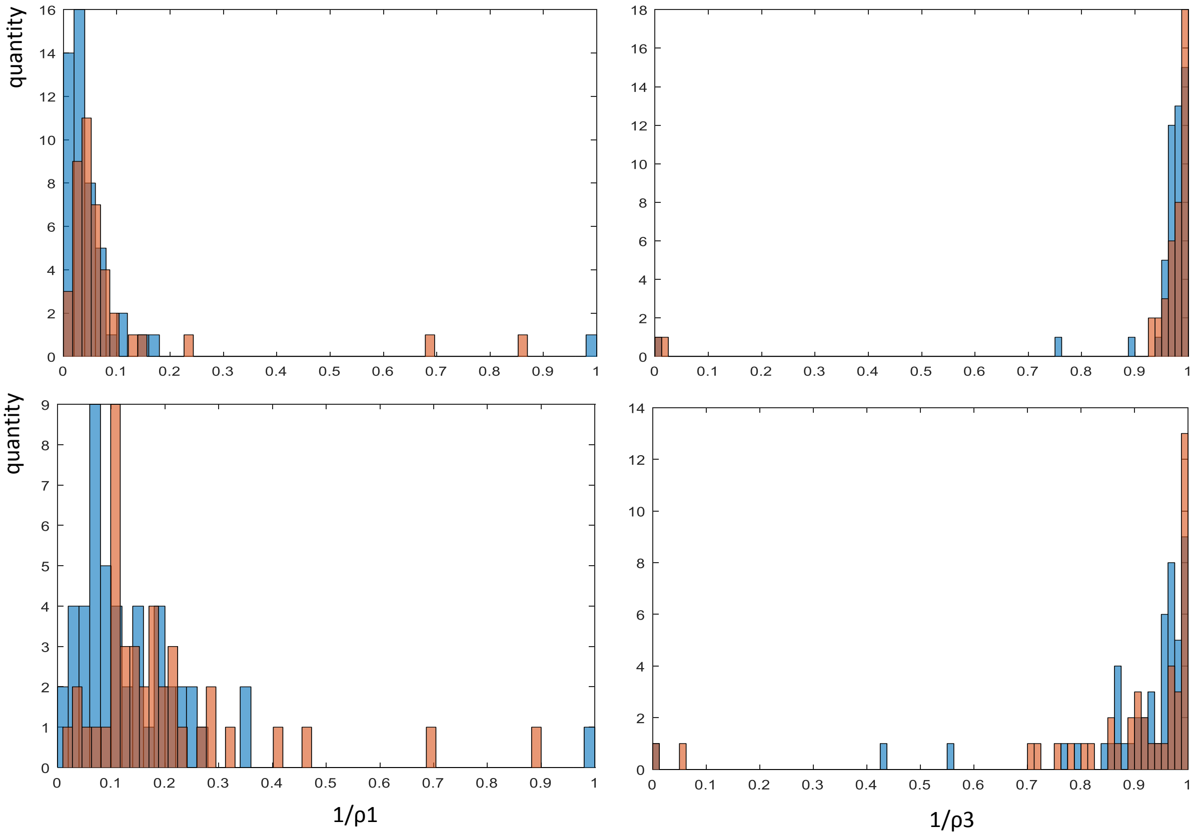

(a)

(b)

Fig. 45 – Normalized scores for 1/ρ1 (top) and 1/ρ3 (bottom): (a) linear normalization; (b) Gaussian normalization

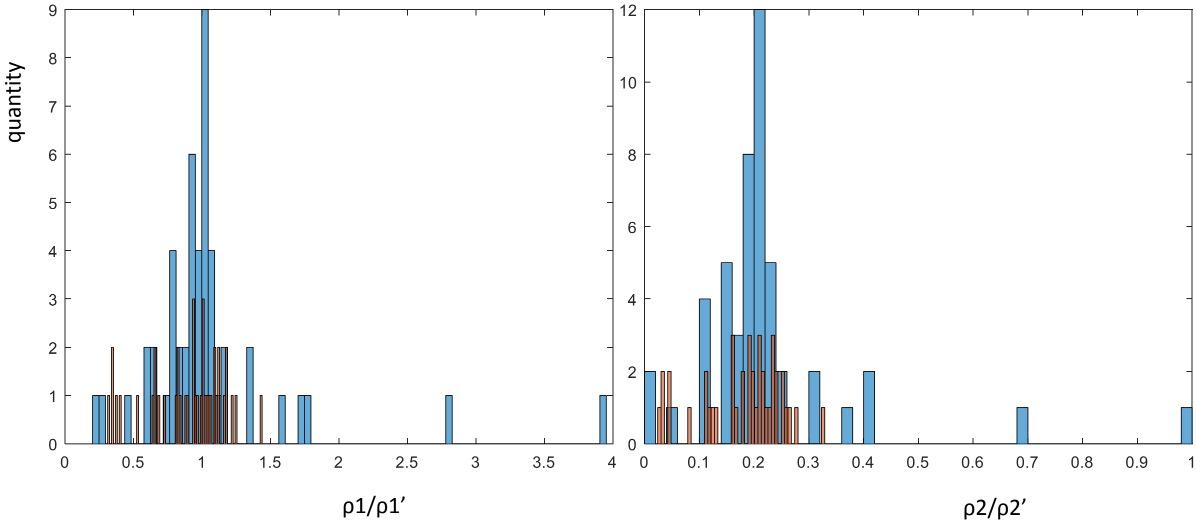

(a)

(b)

Fig. 46- Linearly normalized scores: (a) ρ1/ ρ1’ and (b) ρ2/ ρ2’

11- ALTERED FINGERPRINTS

The external layer of the skin is vulnerable to intentional or intentional alterations and can be changed by some drugs used in the treatment of cancer (DOLEZEL; DRAHANSKY; URBANEK; BREZINOVA; KIM, 2012). These can negatively affect the quality of fingerprints and the performance of fingerprint identification systems as the structure of the ridges and the relative positions of minutiae is affected, as reported by Yoon and Jain (YOON; FENG; JAIN, 2012).

In some cases, the alteration of the fingerprint is done with the intention of masking an individual identity from an identification system by using mechanical (as abrasion or cuts), chemical or even surgical means as shown in the Fig. 47. Cases of successful evasion of border control systems have been reported in the literature (YOON; ZHAO; JAIN, 2012), (SELVARANI; JEBAPRIYA; MARY, 2014) and on a larger scale, fingerprint alteration attempts against the European asylum seeker register, EURODAC have been found (ELLINGSGAARD; SOUSEDIK; BUSCH, 2014)

Fig. 47 – Skin alterations: (a) finger skin replaced by skin from the sole; (2) fingers that were bitten; (c) fingers burnt by acid; (d) stitched fingers; Figure from (YOON; FENG; JAIN, 2012)

In general, according to (YOON; FENG; JAIN, 2012), the alterations can be classified in three categories, obliteration, distortion and imitation: *Obliteration* is the attempt to destroy the fingerprint or part of it by cutting, burning, using chemicals and transplanting the skin from other place of the body. Some cancer treatments can temporarily obliterate fingerprints (HUESO; SANMARTÍN; NAGORE; BOTELLA-ESTRADA; GUILLÉN, 2008). The authors suggest that a countermeasure to obliteration could be the use of dermal fingerprint for identification. *Distortion* is the attempt to change the ridge patterns into unnatural ones by removing parts of the skin and transplanting it to the same finger or to other fingers. This usually results in unusual ridge patterns as abrupt orientation changes or the abnormal distribution of singular points. *Imitation* is the change in the fingerprint that preserves patterns similar to the existing ones in the original fingerprint by removing a piece of skin and stitching together the remaining parts or transplanting entire fingerprints. From the three mentioned, Obliteration is the most popular form of alteration.

Alterations are difficult to detect, in some cases the amount of unreliable minutia found in the fingerprints increases (YOON; ZHAO; JAIN, 2012) but changes not always affect negatively the quality of the fingerprints. In this case, fingerprint quality cannot be used to detect them.

Attempts to detect altered fingerprints using orientation fields and minutiae distribution (YOON; FENG; JAIN, 2012) (SELVARANI; JEBAPRIYA; MARY, 2014); discarding spurious minutiae and restoring minutiae to their original positions in the case of Z-shaped cuts (Fig. 48) or analyzing the singular points density and minutiae orientation (ELLINGSGAARD; SOUSEDIK; BUSCH, 2014) have been published but opportunities for improvement remains as the best false detection rates are in the 2% range. In addition, not all the altered fingerprints can be detected by current methods, as in the case where the altered area is small or when the ridge orientation field and the minutiae density have not been significantly changed an (YOON; FENG; JAIN, 2012).

Fig. 48 – A Z-shaped fingerprint cut. From (YOON; ZHAO; JAIN, 2012). By observing the ridge flow it can be noticed that parts of the skin have been transplanted other positions of the same finger.

During the OCTDB acquisition, some cases of alterations could be observed, as scars, abrasion and cutting, as shown in Fig.49 and Fig.50. In the first case (scar), the external 3D fingerprint shows that the external skin has healed and although some ridge patterns have changed the scar seems not to have affected much the 3D fingerprint. The same is not true for 3D internal fingerprint, the image shows that the deeper layers were strongly affected by the cut, even after healing. In this case, the difference between the internal and external fingerprints could be used to detect the change.

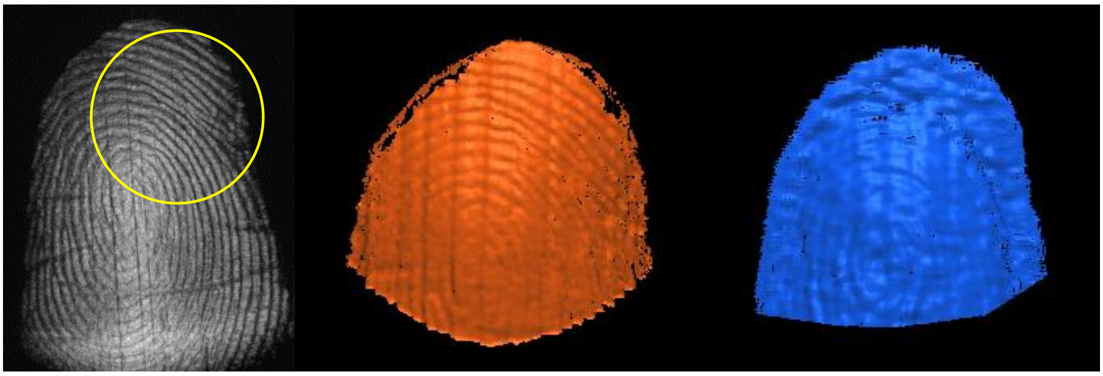

(a) (b) (c)

Fig. 49 – Scar, clearly visible in (a) rendered OCT image;(b) external 3D fingerprint and (c) internal 3D fingerprint strongly affected.

In one experiment, induced alterations using sand paper and a needle to promote a small amount of abrasion in the left middle finger and a small number of scratches on the right ring finger of a volunteer were done, as shown in Fig. 50. Is can be observed that the abrasion had no effect on the outer appearance of the ridges and valleys (left medium finger), but some flattening of the ridges can be observed in the OCT transversal images (B-scans) of the skin (Fig. 50-a). Moreover, the scratches in the right ring finger are clearly visible in the camera picture (Fig. 50-b) and in the OCT transversal images (Fig. 50-c).

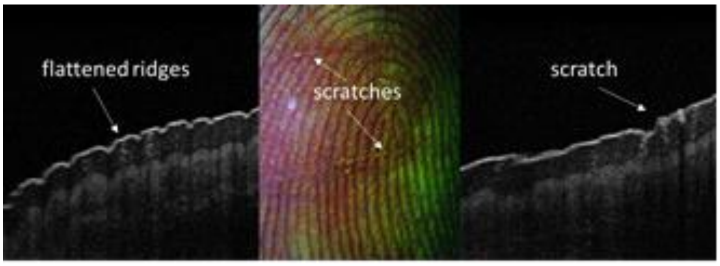

(a) (b) (c)

Fig. 50 – Finger skin damaged by abrasion or scratches. (a) OCT image of ridges flattened by abrasion; (b) scratched skin image; (c) OCT image of scratched ridges

In both cases (abrasion and cut) it can be observed that although some change occurred in the outer layer *(stratum corneum*), the dermis-epidermis junction remains intact. For this reason, it is reasonable to assume that, if the abrasions and scratches are not deep enough to affect the papillary glands, the dermal fingerprint could be detected and used for matching by the proposed method. This practical experiment has shown that shallow abrasion and scratches preserve the dermis-epidermis interface, which may allow the use of dermal 3D fingerprints even in the event of alterations to the outer skin.

Finger Sweating

Another case that could potentially affect the performance of identification systems is the presence of moisture. One of the volunteers had sweating hands and it was possible to capture this condition (shown in Fig.51).

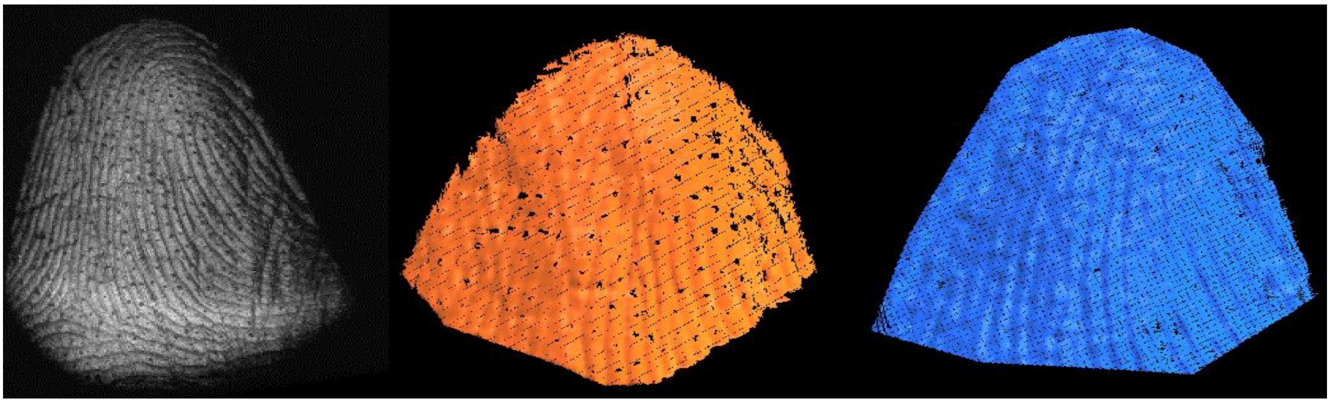

(a) (b) (c)

Fig.51 – Sweating fingers: (a) OCT rendered image; (b) 3D external fingerprint;(c) 3D internal fingerprint

In this case, part of the external fingerprints (around the sweat pores) was affected but the internal fingerprint was unaffected.

Based on the investigated cases, it is reasonable to conclude that cases deep alteration affect both the internal and external fingerprints but superficial changes as scratches, abrasion and some degrees of moisture allow the use of the internal 3D fingerprints for biometric identification. Even in cases of deep alterations, the differences between the internal and external fingerprints (for instance with Iterative Closest Points) can be used to detect potential alterations.

12 - OCT SCANNER PROTOTYPE

One goal of this thesis was to develop a prototype of a OCT scanner for acquiring images of both adults and children (including newborn babies). Part of the research work was developed in a doctoral stage at Stanford University, USA in the Stanford Biomedical Optics Group as this group is one of the centers of excellence in the development of OCT devices. The student scholarship was sponsored by Program Science without Borders/CNPq.

During the research, several design parameters were discussed based on existing implementations, safety recommendations, the IMAGO Research Group and the Stanford Biomedical Optics Group experience and on the nature of the samples, human skin with high light scattering. Other specifications appeared as part of the learning process as more experience with the OCT technology and the scanning of the human skin.

Design Specifications

1) Resolution of 10µm to allow a minimum of 10 points per ridge (as a newborn baby ridge width is approximately 100µm)
2) Sensitivity: approximately 80dB similar to the obtained in (YASUNO; ENDO; MAKITA; AOKI; ITOH; YATAGAI, 2006)
3) Penetration depth: of 500µm as the epidermis depth measures approximately 200µm, according to
4) Field of view: 14mm x 14mm, as used in the obtained in the images of the OCTDB. A resolution x field of view tradeoff may be required.
5) Scanning Speed: 1 to 4 seconds, as used in (LEMES; BELLON; SILVA; JAIN, 2011)
6) Power on the sample smaller than 2mW (following ANSI standard safety recommendations)

Other functional and environmental requirements:

7) Instant image quality feedback is intended to alert to the need to repeat the image acquisition
8) The equipment needs to be portable to fit in surgical centers
9) The equipment needs support sterilization
10) A support for the hand needs is needed to prevent motion artifacts
11) Low cost (compared to commercial OCT scanners)

OCT Implementation

A review of the literature about OCT implementations to image the skin, implementation schemes, key components (as lenses, light sources, spectrometers) and performance parameters served as base to select the implementation alternatives to be implemented, Full-Field OCT and Line-field OCT as detailed in the next session.

Full-field OCT

Full-field OCT a time domain implementation, has the advantage of scanning entire areas (of approximately 16 mm x 16mm) with minimum moving parts as only translation of a mirror is needed for depth scanning. En-Face images (parallel to lens plane) are obtained by collecting images at the desired depth range in steps of a few microns. The final volumetric images are built by stacking the scanned slices. A large amount of slices (hundreds) were needed to obtain a volume of a few millimeters. A first implementation of Full-field OCT (DUBOIS; MONERON; BOCCARA, 2006) based of the architecture described in (FEDERICI, COSTA, OGIEN, ELLERBEE, DUBOIS, 2015) was built in Stanford University with the scheme shown in Fig.52.

The proposed architecture helped reducing costs as a single objective lens were used (instead of a pair of objectives as in the classical implementation of a FF-OCT) and a low cost LED or halogen lamp, were used as light sources. The drawbacks of this architecture were the need to keep the finger very close to the beam splitter (a few millimeters) due to the short objective working distance (what limited the space for placing the finger) and the long acquisition times due to the depth scan (obtained by the translation of the reference mirror) and the need of accumulate images (sum several images at the same depth) to improve the system sensitivity. Usually more than 25 images were needed to generate a single slice, making the acquisition time last several minutes to a single volume. The long acquisition timed impacted the sensitivity due to frequent motion of the finger and the finger images obtained had bad quality.

During the implementation of the FF-OCT, several practical insights occurred as the need to minimize the finger motion due to the long acquisition times are needed to calculate each slice (en-Face image) due to accumulations. Motion also affected the system sensitivity and caused artifacts. An acrylic holder to keep the hand still was built as shown in Fig. 53 but even the use of it did not prevent some motion associated to the difficulty to keep the fingers in the same position during the whole scanning time.

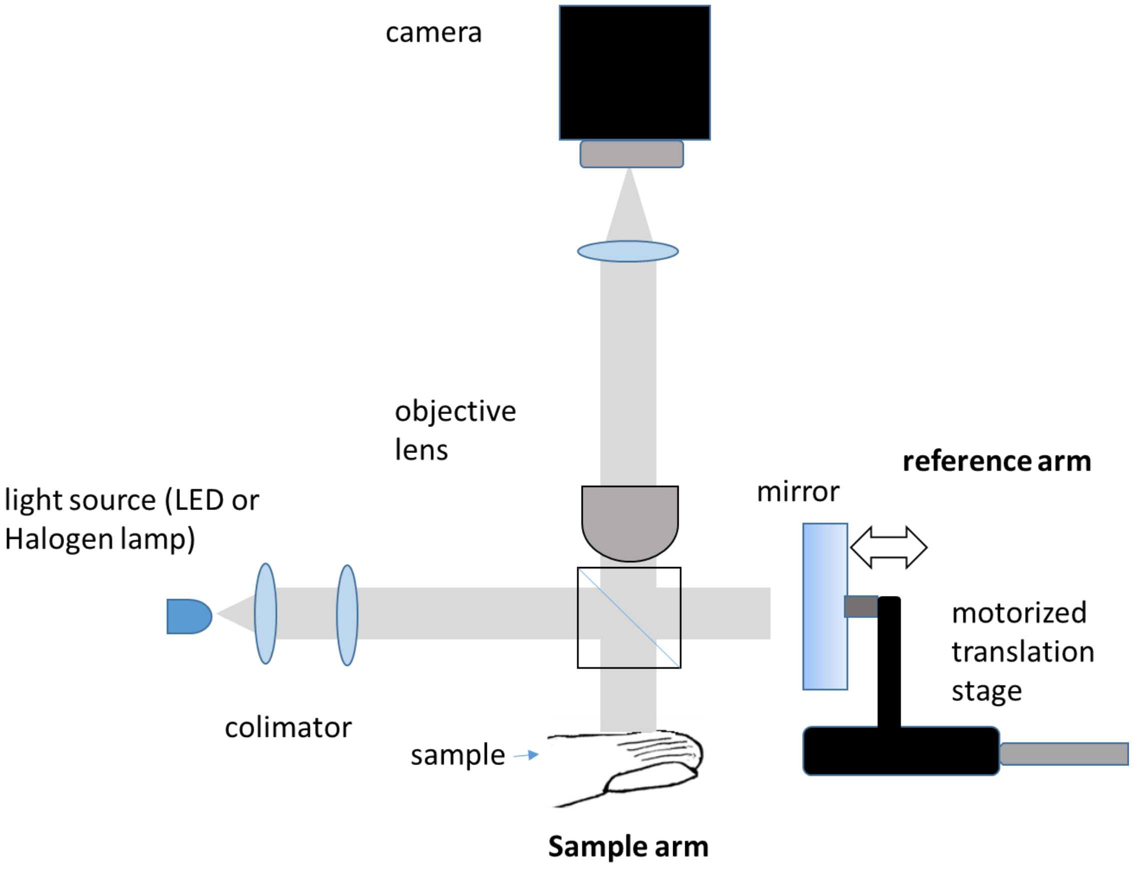

Fig.52 – Full-field OCT implementation schematic

Another insight gained was focusing the objective not on the finger surface but inside the skin and using the reference mirror to scan slices before and after the focused depth in order to explore the whole depth of field (range of depth that keeps the image within an acceptable quality) of the objective lens.

Acceptable images of semi-transparent biological samples as a rat ear (Fig. 54) were obtained but difficulties to obtain images of the finger skin (a scattering media) occurred and only the *stratum corneum* could be imaged due to the low sensitivity obtained. One of the reasons is the presence of motion that made images vanish between successive slice scans as shown in Fig.55.

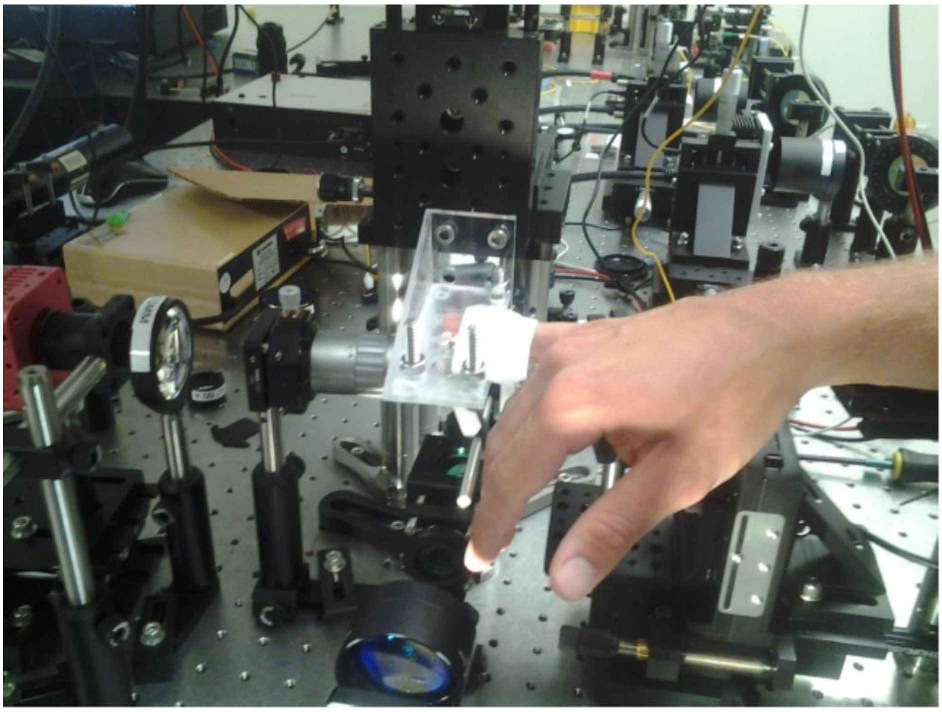

Fig. 53 – FF-OCT prototype

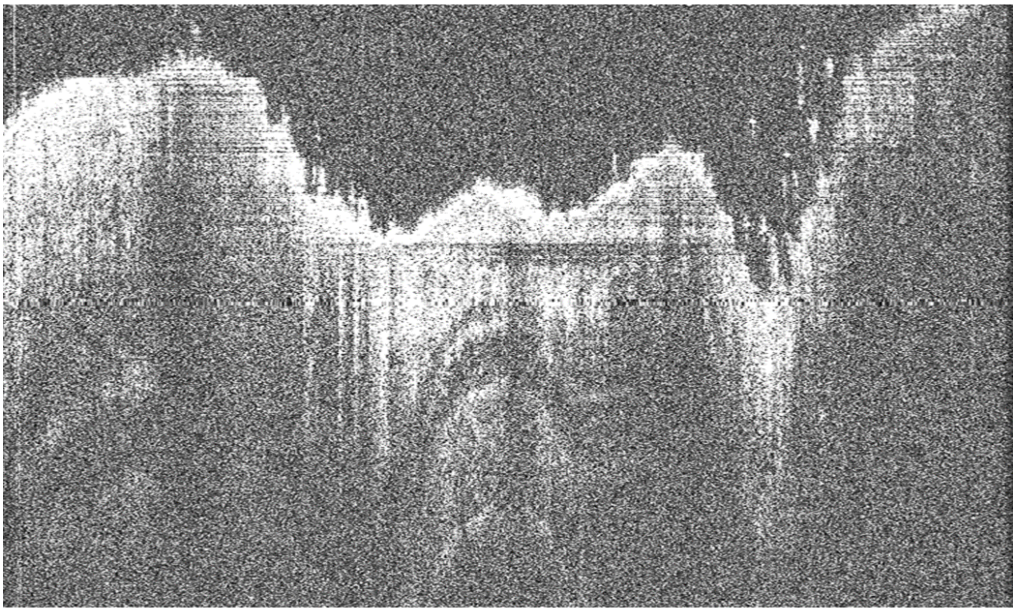

Fig. 54 – A rat ear (B-Scan) imaged with the FF-OCT system

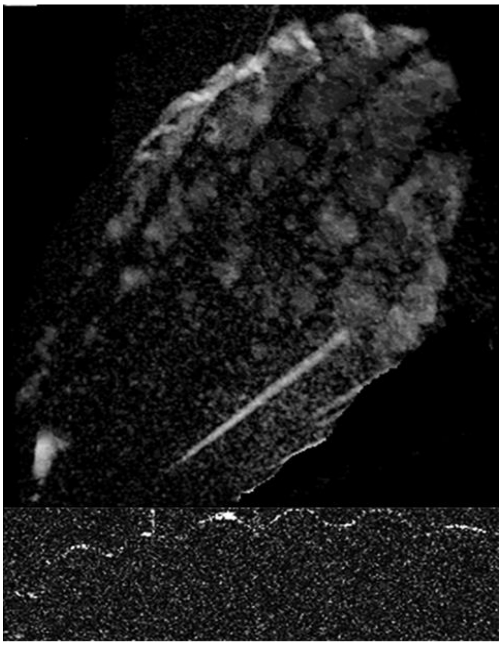

Fig. 55 – FF-OCT images of the finger skin: 3D rendered image of some ridges (top) and a B-scan showing the *stratum corneum* (bottom)

Line- Field OCT

Another implementation studied, named Line-Field OCT and more suited for imaging the skin is currently being tested. This implementation, published in (YASUNO; ENDO; MAKITA; AOKI; ITOH; YATAGAI, 2006) has the advantage of requiring a single rotation to make the scanning beam cover the sample Images of the finger skin have already been obtained (Fig.56), a volume of 2.1mm x 1.4mm x 1.3mm of 480 x 300 x 1024 points in 10s with a sensitivity of 75.6dB and a power on the sample of 1.1mW was reported. In this system, the light beam is shaped as a line and the depth information is recovered through a spectrometer, after processing. Being a FD-OCT, improved sensitivity is expected in relation to the FF-OCT and the faster acquisition times reduce the possibility of motion during the acquisition. One of the drawbacks is the requirement of heavy processing as a Fourier transform is executed to recover the depth information (A-scan) to each point.

A prototype of this scheme is being implemented (Fig. 57) in the IMAGO Research Group laboratories at Universidade Federal do Paraná. One of the differences between this implementation and the on adopted in (YASUNO; ENDO; MAKITA; AOKI; ITOH;

YATAGAI, 2006) is the use of an LED (850nm) as light source instead of a Superluminescent diode (SLD) to minimize costs. A Photonfocus Gigabit camera with 1312 x 1082 pixels was adopted.

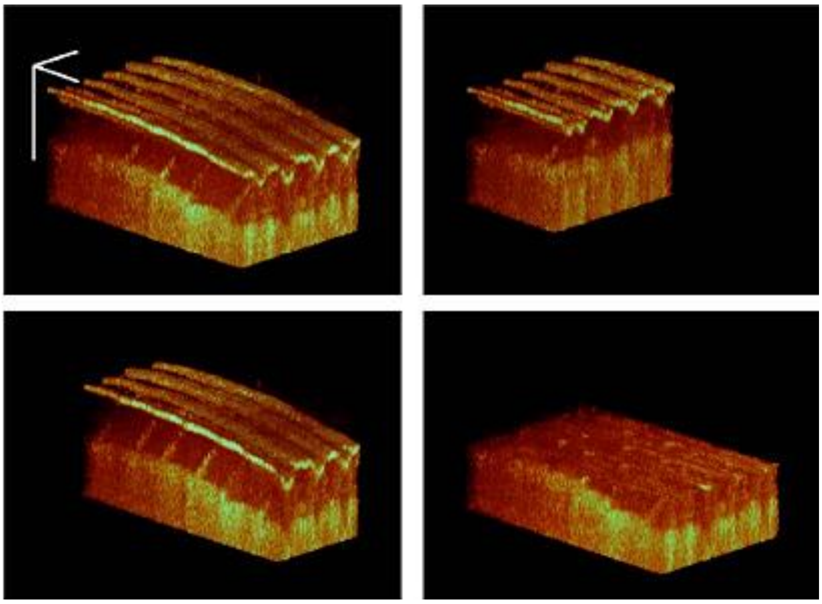

Fig. 56 – Skin images acquired by a Line-field OCT device (YASUNO, ENDO, MAKITA, AOKI, ITOH,YATAGAI, 2006)

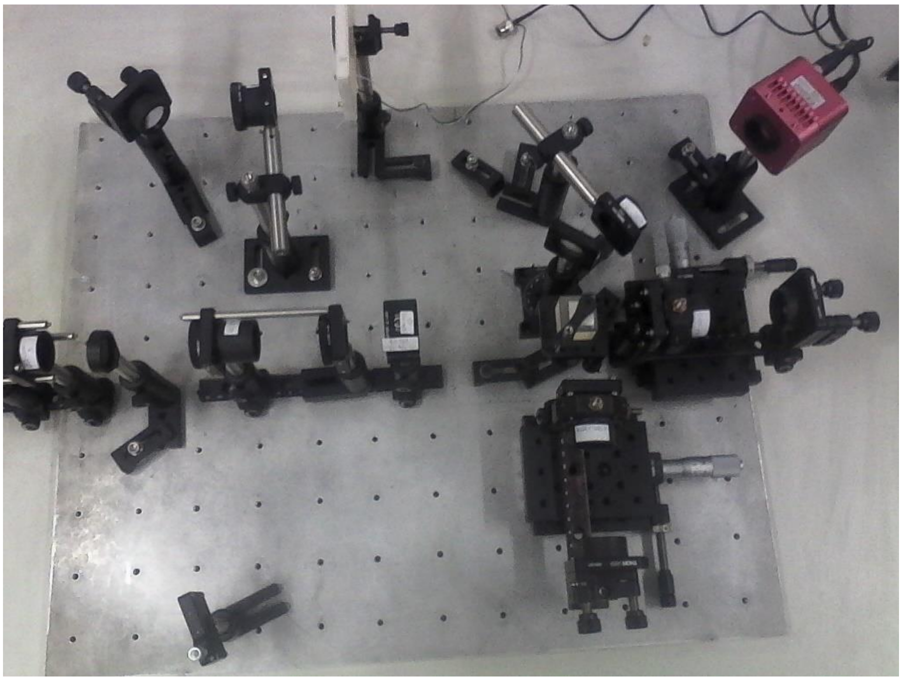

Fig. 57 – Prototype being implemented in IMAGO Research Group laboratory (Universidade Federal do Paraná)

The next steps to the prototype implementation are the installation of new translation stages to increase the degrees of freedom of the system, the improvement of focusing the LED light on the sample by optimizing the beam diameter, the adoption of a slit between the beam splitter and the diffraction grating to reject light out of focus from the sample and the use of a ND (neutral density) filter to balance the power between the reference and sample arms as in (WANG; DAINTY; PODOLEANU, 2009). B-scans of test samples will be scanned and the installation of a galvo mirror will be added to collect volumes. Follows performance optimization, usability improvements and a future miniaturization of the system.

13 – CONCLUSIONS AND FUTURE DIRECTIONS

The acquisition of 3D fingerprints obtained through the use of Optical Coherence Tomography was proved viable and the first OCT 3D fingerprint database to date, containing 163 3D fingerprints from eleven volunteers of different genders, ethnicity and skin conditions was obtained. This database allows the exploitation of novel features and structures as papillary glands and sweat ducts for improved matching. A 2D database from the same group of volunteers was also obtained to allow a comparison with existing matching methods.

OCT has a series of advantages over the multi-camera triangulation-based and structured illumination profilometry-based systems as the immunity to contrast and illumination problems and reconstruction errors. Besides that, the access to the internal layers of the skin opens the possibility to do biometric identification and matching in the presence of alterations, moisture or when the external layer of the skin is not accessible.

A new matching method, based on new features, the KH maps, computed from small selected regions of the 3D fingerprint, the minutiae clouds, was proposed to improve the biometric identification accuracy. A two-step LGP-based matching process was devised to cope with the large volume of minutiae clouds obtained and reduced the processing time by 85%. These matching results, for two databases, the OCTDB and a publicly available database (POLYUDB), were tested and a comparison with 2D traditional matching for the same volunteers was executed. Identification rates of 75% and 77.61 % and EER of 12.77% and 12.36% for respectively the OCTDB and POLYUDB to a single minutiae cloud and 94.23% and 99% for an EER 0f 0.09% and 0.01% for multiple minutiae were achieved.

The case of matching an external 3D database (gallery) using internal fingerprints (probe) has been tested obtaining identification rate of 88.89% and EER 0f 0.06% showing that identification is feasible when only the internal fingerprint is available, as in the case of alterations. Practical cases of alterations as scars, abrasion and cuts and a condition of excessive moisture were analyzed to check the impact of such conditions in the 3D internal fingerprints.

A set of three 3D quality indicators related to density and smoothness was proposed and their efficacy to promote the separation of classes match and no match was evaluated for the mentioned databases using different normalization schemes.

The description of the parameters of a Full-Field (Time Domain) prototype, built in Stanford University, tests with fingerprint scanning and practical insights gained during the experiments is presented and details of a Line-field (FD-OCT) scanner prototype (in construction), customized to scanning 3D fingerprints in adults and babies is presented and its parameters evaluated.

As future directions, the construction of larger 3D fingerprint databases including more cases of alteration is intended and a more detailed evaluation of varied degrees of moisture and dirt are intended. The evaluation of the use of other types of minutiae clouds as cores and deltas is intended as the prototype is finished. A test with different kinds of dirt in the hands to evaluate the potential of the technology in the case of disasters or catastrophes that resulted in damage to the fingerprints.

The current database will be used with future research as improvements in the 3D fingerprint acquisition process, extraction of minutiae clouds, in the matching speed and the test of new 3D matching methods using iterative closest points (ICP) and Surface interpenetration Measure (SILVA; BELLON; BOYER, 2005).The evaluation of the impact of using the quality indicators as predictors of performance is also feasible.

Finally, an acquisition of children fingerprints, when the prototype conclusion and the safety conditions are assured is intended.

REFERENCES

ABAZA, A.; BOURLAI, T.; ROSS, A.; HARRISON, M. A. Design and evaluation of photometric image quality measures for effective face recognition. **IET Biometrics**, v. 3, n. 4, p. 314–324, 2014.

ABAZA, A.; HARRISON, M.; BOURLAI, T. **Quality metrics for practical face recognition**. Proceedings of Pattern Recognition (ICPR), …. **Anais**...2012Disponível em: <http://ieeexplore.ieee.org/xpls/abs_all.jsp?arnumber=6460821>

AUKSORIUS, E.; BOCCARA, A. C. Fingerprint imaging from the inside of a finger with full-field optical coherence tomography. **Biomedical Optics Express**, v. 6, n. 11, p. 4465, 2015.

AVANAKI, M. R. N.; HOJJATOLESLAMI, A. Skin layer detection of optical coherence tomography images. **Optik - International Journal for Light and Electron Optics**, v. 124, n. 22, p. 5665–5668, nov. 2013.

BENTLEY, J. L. Multidimensional binary search trees used for associative searching. **Communications of the ACM**, v. 18, n. 9, p. 509–517, 1975.

BESL, P. J. **Surfaces in Range Image Understanding**. First Edit ed. [s.l.] Springer-Verlag, 1988.

BESL, P. J.; JAIN, R. Invariant Surface Characteristics for 3D Object Recognition in Range Images. **Computer Vision, Graphics and Image Processing**, v. 33, p. 33–80, 1986.

BOUMA, B.E.TEARNEY, G. J. **Handbook of Optical Coherence Tomography**. New York: Marcel Dekker AG, 2002.

BREITHAUPT, R.; SOUSEDIK, C.; MEISSNER, S. **Full fingerprint scanner using optical coherence tomography**. Biometrics and Forensics (IWBF), 2015 International Workshop on. **Anais**...IEEE, 2015

CANNY, J. A computational approach to edge detection. **IEEE Transactions on Pattern Analysis and Machine Intelligence**, v. 8, n. 6, p. 679–698, 1986.

CHANG, S.; XIAOQING, D. Multi-biometrics fusion for identity verification. **Proceedings - International Conference on Pattern Recognition**, v. 4, p. 493–496, 2006.

CHEN, Y.; PARZIALE, G.; DIAZ-SANTANA, E.; JAIN, A. K. **3D Touchless**

Fingerprints: Compatibility with Legacy rolled Images. (IEEE, Ed.)Biometrics Consortium Biometrics Symposium. **Anais**...2006

CHENG, Y.; LARIN, K. V. Artificial fingerprint recognition by using optical coherence tomography with autocorrelation analysis. **Applied optics**, v. 45, n. 36, p. 9238–45, 20 dez. 2006.

COSTA, H. S. G.; BELLON, O. R. P.; SILVA, L.; BOWDEN, A. K. **Towards Biometric Identification Using 3D Epidermal and Dermal Fingerprints**. (IEEE Signal Processing Society, Ed.)IEEE International Conference on Image Processing. **Anais**...Phoenix: IEEE Signal Processing Society, 2016

CUMMINS, H.; MIDLO, C. **Finger Prints, Palms and Soles**. New York: Dover Publications Inc., 1976.

D.MALTONI, A.JAIN, D.MAIO, S. P. **Handbook of Fingerprint Recognition**. First Edit ed. New York: Springer, 2003.

DARLOW, L. N.; CONNAN, J. Efficient internal and surface fingerprint extraction and blending using optical coherence tomography. **Journal of Electronic Imaging**, v. 54, n. 31, p. 9258–9268, 2015.

DOLEZEL, M.; DRAHANSKY, M.; URBANEK, J.; BREZINOVA, E.; KIM, T. Influence of Skin Diseases on Fingerprint Quality and Recognition. In: YAN, J. (Ed.). . **New Trends and Developments in Biometrics**. InTech ed. [s.l.] InTech, 2012. p. 275–298.

DREXLER, W.; FUJIMOTO, J. **Optical Coherence Tomography: Technology and Applications**. New York, USA: [s.n.].

DUBOIS, ARNAUD;BOCCARA, A. C. **Optical Coherence Tomography**. 1. ed. Berlin, Heidelberg: Springer Berlin Heidelberg, 2008.

DUBOIS, A. Full-Field Optical Coherence Microscopy. In: **Handbook of Optical Coherence Tomography**. [s.l.] CRC Press, 2001. p. 299–333.

DUBOIS, A.; MONERON, G.; BOCCARA, C. Thermal-light full-field optical coherence tomography in the 1.2µm wavelength region. **Optics Communications**, v. 266, n. 2, p. 738–743, out. 2006.

DUBOIS, A.; VABRE, L.; BOCCARA, A.-C.; BEAUREPAIRE, E. High-resolution full-field optical coherence tomography with a Linnik microscope. **Applied optics**, v. 41, n. 4, p.

805–12, 1 fev. 2002.

ELLINGSGAARD, J.; SOUSEDIK, C.; BUSCH, C. **Detecting fingerprint alterations by orientation field and minutiae orientation analysis**. 2nd International Workshop on Biometrics and Forensics. **Anais**...IEEE, mar. 2014Disponível em: <http://ieeexplore.ieee.org/lpdocs/epic03/wrapper.htm?arnumber=6914240>

FEDERICI, A.; GUTIERREZ DA COSTA, H. S.; OGIEN, J.; ELLERBEE, A. K.; DUBOIS, A. Wide-field, full-field optical coherence microscopy for high-axial-resolution phase and amplitude imaging. **Applied Optics**, v. 54, n. 27, p. 8212, 2015.

FENG, J.; JAIN, A. K.; ROSS, A. Detecting Altered Fingerprints. **2010 20th International Conference on Pattern Recognition**, p. 1622–1625, ago. 2010.

FERCHER, A. F. Optical coherence tomography - development, principles, applications. **Zeitschrift fur medizinische Physik**, v. 20, n. 4, p. 251–276, jan. 2010.

FERCHER, A. F.; DREXLER, W.; HITZENBERGER, C. K.; LASSER, T. Optical coherence tomography - principles and applications. **Reports on Progress in Physics**, v. 66, n. 2, p. 239–303, 1 fev. 2003.

FUJIMOTO, J. G. Optical coherence tomography imaging: Technology and applications. **2011 Conference on Lasers and ElectroOptics Europe and 12th European Quantum Electronics Conference CLEO EUROPEEQEC**, p. 1–1, 2006.

FVC2004: the Third International Fingerprint Verification Competition. Disponível em: <http://bias.csr.unibo.it/fvc2004/results.asp>.

GALBALLY, J.; CAPPELLI, R.; LUMINI, A.; GONZALEZ-DE-RIVERA, G.; MALTONI, D.; FIERREZ, J.; ORTEGA-GARCIA, J.; MAIO, D. An evaluation of direct attacks using fake fingers generated from ISO templates. **Pattern Recognition Letters**, v. 31, n. 8, p. 725–732, jun. 2010.

GAMBICHLER, T.; MATIP, R.; MOUSSA, G.; ALTMEYER, P.; HOFFMANN, K. In vivo data of epidermal thickness evaluated by optical coherence tomography: effects of age, gender, skin type, and anatomic site. **Journal of dermatological science**, v. 44, n. 3, p. 145–52, dez. 2006.

GAMBICHLER, T.; MOUSSA, G.; SAND, M.; SAND, D.; ALTMEYER, P.; HOFFMANN, K. Applications of optical coherence tomography in dermatology. **Journal of dermatological science**, v. 40, n. 2, p. 85–94, nov. 2005.

GONZALEZ, RAFAEL C.;WOODS, RICHARD E.;EDDINS, S. L. **Digital Image Processing using MATLAB**. 1st. ed. New Jersey: Pearson Prentice Hall, 2004.

GUTIERREZ DA COSTA, H. S.; MAXEY, J. R.; SILVA, L.; ELLERBEE, A. K. **Evaluation of fingerprint deformation using optical coherence tomography**. (SPIE, Ed.)SPIE Photonics West Conference. **Anais**...San Francisco: SPIE, 2014

HECHT, E. **Optics**. 4th. ed. San Francisco: Addison Wesley, 2002.

HOJJATOLESLAMI, A.; AVANAKI, M. R. N. OCT skin image enhancement through attenuation compensation. **Applied Optics**, v. 51, n. 21, p. 4927–4935, 20 jul. 2012.

HUANG, S.; ZHANG, Z.; ZHAO, Y.; DAI, J.; CHEN, C.; XU, Y.; ZHANG, E.; XIE, L. 3D fingerprint imaging system based on full-field fringe projection profilometry. **Optics and Lasers in Engineering**, v. 52, p. 123–130, 2014.

HUESO, L.; SANMARTÍN, O.; NAGORE, E.; BOTELLA-ESTRADA, R.; REQUENA, C.; LLOMBART, B.; SERRA-GUILLÉN, C.; ALFARO-RUBIO, A; GUILLÉN, C. Chemotherapy-induced acral erythema: a clinical and histopathologic study of 44 cases. **Actas dermo-sifiliograficas**, v. 99, n. 4, p. 281–290, 2008.

JAIN, A.; ABRAMOVICH, G. **3D to 2D fingerprints: Unrolling and distortion correction**. International Joint Conference on Biometrics (IJCB). **Anais**...IEEE, out. 2011Disponível em: <http://ieeexplore.ieee.org/lpdocs/epic03/wrapper.htm?arnumber=6117585>

JAIN, A. K.; ROSS, A.; PRABHAKAR, S. An Introduction to Biometric Recognition. **IEEE Transactions on Circuits and Systems for Video Technology**, v. 14, n. 1, p. 4–20, jan. 2004.

JUN, B.; KIM, D. Robust face detection using local gradient patterns and evidence accumulation. **Pattern Recognition**, v. 45, n. 9, p. 3304–3316, 2012.

KANG, D.-S. Robust Face Detection Using Uniform Local Gradient Pattern (ULGP) and AdaBoost Algorithm. **2015 4th International Conference on Modeling and Simulation (MAS)**, v. 0, n. 2, p. 13–16, 2015.

KARNA, D. K.; AGARWAL, S.; NIKAM, S. **Normalized cross-correlation based fingerprint matching**. Proceedings - Computer Graphics, Imaging and Visualisation, Modern Techniques and Applications, CGIV. **Anais**...2008

KNUTTEL, K.; BONEV, S.; KNAAK, W. **Scattering and refractive index properties of skin obtained with OCT**. Proceedings of the SPIE-OSA Biomedical Optics. **Anais**...2003

KUMAR, A. **The Hong Kong Polytechnic University 3D Fingerprint Images Database**. Disponível em: <http://www4.comp.polyu.edu.hk/~csajaykr/3Dfingerprint.htm>. Acesso em: 1 jan. 2015.

KUMAR, A.; KWONG, C. **Towards contactless, low-cost and accurate 3D fingerprint identification**. Proceedings of the IEEE Computer Society Conference on Computer Vision and Pattern Recognition. **Anais**...2013

KUMAR, A.; KWONG, C. Towards Contactless, Low-Cost and Accurate 3D Fingerprint Identification. **IEEE Transactions on Pattern Analysis and Machine Intelligence**, v. 37, n. 3, p. 681–696, jun. 2015.

LABATI, R. D.; GENOVESE, A.; PIURI, V.; SCOTTI, F. Toward Unconstrained Fingerprint Recognition : A Fully Touchless 3-D System Based on Two Views on the Move. **IEEE Transactions on Systems, Man and Cybernetics**, v. 46, n. 2, p. 202–219, 2016.

LEITGEB, R.; HITZENBERGER, C.; FERCHER, A. Performance of fourier domain vs. time domain optical coherence tomography. **Optics Express**, v. 11, n. 8, p. 889–894, 2003.

LEMES, R. P.; BELLON, O. R. P.; SILVA, L.; JAIN, A. K. Biometric recognition of newborns: Identification using palmprints. **2011 International Joint Conference on Biometrics (IJCB)**, p. 1–6, out. 2011.

LI, S.; JAIN, A. K. **Encyclopedia of Biometrics**. First Edit ed. New York, USA: Springer Science+Business Media, 2009.

LIU, F.; ZHANG, D. 3D fingerprint reconstruction system using feature correspondences and prior estimated finger model. **Pattern Recognition**, v. 47, n. 1, p. 178–193, 2014.

LIU, F.; ZHANG, D.; SHEN, L. Study on novel Curvature Features for 3D fingerprint recognition. **Neurocomputing**, p. 1–10, 2015.

LUBING, Z.; HAN, W. **Local Gradient Increasing Pattern for Facial Expression Recognition**. 2012 19th IEEE International Conference on Image Processing. **Anais**...Orlando: 2012

MEISSNER, S.; BREITHAUPT, R.; KOCH, E. Defense of fake fingerprint attacks using a swept source laser optical coherence tomography setup. v. 8611, p. 86110L–86110L–4, 15 mar. 2013a.

MEISSNER, S.; BREITHAUPT, R.; KOCH, E. Fingerprint fake detection by optical coherence tomography. v. 8571, p. 85713L–85713L–4, 20 mar. 2013b.

MIZOKAMI, L. L.; SILVA, L. R. V.; KÜCKELHAUS, S. A. S. Comparison between fingerprints of the epidermis and dermis: Perspectives in the identifying of corpses. **Forensic Science International**, v. 252, p. 77–81, 2015.

NASIRI-AVANAKI, M.-R. Anti-Spoof Reliable Biometry of Fingerprints Using *En-Face* Optical Coherence Tomography. **Optics and Photonics Journal**, v. 01, n. 03, p. 91–96, 2011.

NEUROTECHNOLOGY. **Fingerprint Verification Algorithm Demo Application**. Disponível em: <http://www.neurotechnology.com/download.html#demo>. Acesso em: 6 fev. 2016.

NIST. **NIST Biometric Image Software**. Disponível em: <http://www.nist.gov/itl/iad/ig/nbis.cfm>.

PARZIALE, G. Touchless Fingerprinting Technology. In: RATHA, NALINI; GOVINDARAJU, V. (Ed.). . **Advances in Biometrics - Sensors , Algorithms and Systems**. [s.l.] Springer, 2008. p. 25–48.

PARZIALE, G.; DIAZ-SANTANA, E.; HAUKE, R. The Surround Imager : a multi-camera touchless device to acquire 3D rolled-equivalent fingerprints. **International Conference on Advances in Biometrics, ICB 2006**, v. LNCS 3832, p. 244–250, 2005.

POH, N.; ROSS, A.; LEE, W.; KITTLER, J. A user-specific and selective multimodal biometric fusion strategy by ranking subjects. **Pattern Recognition**, v. 46, n. 12, p. 3341–3357, 2013.

SELVARANI, S.; JEBAPRIYA, S.; MARY, R. S. Automatic Identification and Detection of Altered Fingerprints. **2014 International Conference on Intelligent Computing Applications**, p. 239–243, 2014.

SILVA, L.; BELLON, O. R. P.; BOYER, K. L. Precision Range Image Registration Using a Robust Surface Interpenetration Measure and Enhanced Genetic Algorithms. **IEEE Transactions on Pattern Analisys and Machine Intelligence**, v. 27, n. 5, p. 762–776, 2005.

SILVA, L.; BELLON, O. R. P.; GOTARDO, P. F. U. **Edge-based image segmentation**

using curvature sign maps from reflectance and range images. Proceedings 2001 International Conference on Image Processing (Cat. No.01CH37205). **Anais**...IEEE, 2001Disponível em: <http://ieeexplore.ieee.org/lpdocs/epic03/wrapper.htm?arnumber=959149>

THORLABS. **Thorlabs - Scan Lenses for Laser Scanning Microscopy**. Disponível em: <https://www.thorlabs.com/newgrouppage9.cfm?objectgroup_id=2910&pn=LSM03>. Acesso em: 1 jan. 2016.

VENUS, M.; WATERMAN, J.; MCNAB, I. Basic physiology of the skin. **Surgery (Oxford)**, v. 28, n. 10, p. 469–472, out. 2010.

WANG, J.; DAINTY, C.; PODOLEANU, A. **Line-field Spectral Domain Optical Coherence Tomography using a 2D Camera**. Proceedings of SPIE-OSA Biomedical Optics. **Anais**...2009Disponível em: <http://proceedings.spiedigitallibrary.org/proceeding.aspx?articleid=781252>

WANG, Y.; HASSEBROOK, L. G.; LAU, D. L. Data acquisition and processing of 3-D fingerprints. **IEEE Transactions on Information Forensics and Security**, v. 5, n. 4, p. 750–760, 2010.

WEINGAERTNER, D. (UFPR). **Aquisição de Impressões Palmares em Formato Digital para a Identificação Biométrica de Recém-Nascidos**. [s.l.] Universidade Federal do Paraná, 2007.

WOJTKOWSKI, M. High-speed optical coherence tomography: basics and applications. **Applied Optics**, v. 49, n. 16, p. D30–D61, 2010.

WOJTKOWSKI, M.; SRINIVASAN, V. J.; KO, T. H.; FUJIMOTO, J. G.; KOWALCZYK, A.; DUKER, J. S. Ultrahigh-resolution, high-speed domain optical coherence tomography and methods for dispersion compensation. **Optics express**, v. 12, n. 11, p. 707–709, 2004.

YANG, B.-W.; CHEN, X.-C. Full-color skin imaging using RGB LED and floating lens in optical coherence tomography. **Biomedical optics express**, v. 1, n. 5, p. 1341–1346, jan. 2010.

YASUNO, Y.; ENDO, T.; MAKITA, S.; AOKI, G.; ITOH, M.; YATAGAI, T. Three-dimensional line-field Fourier domain optical coherence tomography for in vivo dermatological investigation. **Journal of biomedical optics**, v. 11, n. 1, p. 014014, 2006.

YASUNO, Y.; MAKITA, S.; ENDO, T.; AOKI, G.; NAKAMURA, Y.; YAMANARI, M.; ITOH, M.; YATAGAI, T. Standard and line-field fourier domain optical coherence tomography. **Conf Proc IEEE Eng Med Biol Soc**, v. 7, p. 7224–7226, 2005.

YOON, S.; FENG, J.; JAIN, A. K. Altered fingerprints: analysis and detection. **IEEE Transactions on Pattern Analysis and Machine Intelligence**, v. 34, n. 3, p. 451–64, mar. 2012.

YOON, S.; ZHAO, Q.; JAIN, A. K. **On matching altered fingerprints**. Proceedings - 2012 5th IAPR International Conference on Biometrics, ICB 2012. **Anais**...2012

ZAKHAROV, P.; TALARY, M. S.; KOLM, I.; CADUFF, A. **Rapid skin profiling with non-contact full-field optical coherence tomography: Study of patients with diabetes mellitus type I**. (SPIE, Ed.)Proceedings of SPIE-OSA Biomedical Optics - Optical Coherence Tomography and Coherence Techniques. **Anais**...SPIE, 2009Disponível em: <http://dx.doi.org/10.1117/12.831838>

ZHAO, G.; PIETIKAINEN, M. Dynamic Texture Recognition Using Local Binary Patterns with an Application to Facial Expressions. **IEEE transactions on pattern analysis and machine intelligence**, v. 29, n. 6, p. 915–928, 2007.